

## Two-Component $\gamma$ -ray Emission Spectrum and X-Ray Polarization of the Radio Galaxy Pictor A

JIA-XUAN LI,<sup>1</sup> XIN-KE HU,<sup>1</sup> JI-SHUN LIAN,<sup>1</sup> YU-WEI YU,<sup>1</sup> WEI DENG,<sup>2</sup> KUAN LIU,<sup>2</sup> HAI-MING ZHANG<sup>†</sup>,<sup>2</sup> LIANG CHEN,<sup>3</sup>  
AND JIN ZHANG<sup>†</sup><sup>1</sup>

<sup>1</sup>*School of Physics, Beijing Institute of Technology, Beijing 100081, People's Republic of China; j.zhang@bit.edu.cn*

<sup>2</sup>*Guangxi Key Laboratory for Relativistic Astrophysics, School of Physical Science and Technology, Guangxi University, Nanning 530004, People's Republic of China; hmzhang@gxu.edu.cn*

<sup>3</sup>*Key Laboratory for Research in Galaxies and Cosmology, Shanghai Astronomical Observatory, Chinese Academy of Sciences, 80 Nandan Road, Shanghai 200030, People's Republic of China*

### ABSTRACT

Pictor A is a  $\gamma$ -ray emitting radio galaxy and has a bright hotspot called WHS, located  $\sim 4$  arcmin away from the nucleus. In this work, we present an analysis of its 16-year Fermi-LAT data and report the Imaging X-ray Polarimetry Explorer (IXPE) observations for this source. Our analysis of the Fermi-LAT observations reveals evidence of two components in the average  $\gamma$ -ray spectrum of Pictor A, exhibiting a statistically significant hardening from  $\Gamma_{\gamma,1} = 3.25 \pm 0.15$  to  $\Gamma_{\gamma,2} = 1.81 \pm 0.07$  at a break energy of  $2.46 \pm 0.09$  GeV. Notably, variability of  $\gamma$ -rays is evident in Pictor A, predominantly driven by the component below the break energy, while the component above the break energy remains stable. Furthermore, our analysis reveals that a power-law function provides an adequate fit for the high-flux-state spectrum, while a broken power-law function remains necessary to accurately model the low-flux-state spectrum. We suggest that the low-energy component originates from the nucleus, while the high-energy component primarily stems from WHS. The broadband spectral energy distributions of both nucleus and WHS can be well represented by a simple leptonic model, with both  $\gamma$ -ray components attributed to the synchrotron-self-Compton (SSC) process. Analysis of IXPE data provides upper limits on the polarization degree of  $\Pi_X < 6.6\%$  for the nucleus and  $\Pi_X < 56.4\%$  for the WHS within the 2–8 keV band. For the nucleus, this result aligns with X-ray emission originating from the SSC process. However, the upper limit of  $\Pi_X < 56.4\%$  for WHS is insufficient to conclusively determine the X-ray emission mechanism in this region.

*Keywords:* galaxies: active—galaxies: jets—radio continuum: galaxies—gamma rays: galaxies—X-ray: polarimetry

### 1. INTRODUCTION

Radio galaxies (RGs), a subset of radio-loud Active Galactic Nuclei (RL-AGNs), are distinguished by the presence of jet substructures that extend from the radio core to scales of kiloparsecs to megaparsecs (kpc–Mpc). Hotspots, characterized by high surface brightness at the edges of extended radio lobes in RGs, are considered to represent the jet termination, where magnetic fields are amplified and particles are accelerated to high energies (Meisenheimer et al. 1989; Thimmappa et al. 2022). Thanks to Chandra observations, numer-

ous hotspots and knots within RG jets have been detected in the X-ray band (Harris & Krawczynski 2006 for a review), however, ongoing debate persists regarding their X-ray radiation mechanisms (e.g., Kataoka & Stawarz 2005; Zhang et al. 2010, 2018). For substructures characterized by a hard X-ray spectrum, the X-ray emission is likely produced by inverse Compton scattering (IC) from relativistic electrons that are responsible for the radio-optical emission via the synchrotron process (e.g., Tavecchio et al. 2000, 2005; Georganopoulos & Kazanas 2003; Stawarz et al. 2007; Zhang et al. 2010, 2018), or alternatively by synchrotron radiation from a second population of high-energy particles (e.g., Thimmappa et al. 2020; Wang et al. 2020; Sunada et al. 2022; He et al. 2023).

In addition, both the IC and second synchrotron radiation models of X-rays predict the observable  $\gamma$ -ray emission for some large-scale jet substructures (Zhang et al. 2010, 2018; Wang et al. 2020; He et al. 2023). The detection of  $\gamma$ -rays from large-scale radio lobes of RGs Cen A (Abdo et al. 2010; Sun et al. 2016; H. E. S. S. Collaboration et al. 2020), Fornax A (Ackermann et al. 2016), and NGC 6251 (Yu et al. 2024) confirms that the large-scale jet substructures are acceleration sites of high-energy particles. To date, the Fermi Large Area Telescope (Fermi-LAT) has detected numerous RGs (Abdollahi et al. 2022; Ballet et al. 2023); however, the limited spatial resolution of Fermi-LAT makes it difficult to judge the location of the  $\gamma$ -ray emission for the majority of RGs. It has been proposed that some large-scale jet substructures may have the detectable  $\gamma$ -ray emission through the search for a steady  $\gamma$ -ray emission component and modeling of the broadband spectral energy distributions (SEDs; Guo et al. 2018; Zhang et al. 2018).

Polarization measurements serve as a valuable tool for evaluating the radiation mechanisms of X-rays. The launch of the Imaging X-ray Polarimetry Explorer (IXPE; Weisskopf 2022) has enabled this assessment to become feasible. Due to the high brightness of RL-AGNs, they constitute one of the primary observation targets for IXPE, particularly blazars (e.g., Liodakis et al. 2022; Di Gesu et al. 2022; Middei et al. 2023a,b; Ehlert et al. 2023; Errando et al. 2024; Kouch et al. 2024; Marshall et al. 2024). The first RG observed by IXPE was Cen A (Ehlert et al. 2022); however, no statistically significant degree of polarization was detected. Only an upper limit of 6.5% was established for the core region, and insufficient counts were obtained to measure statistically significant X-ray polarization from the X-ray jet. Recently, IXPE has observed the second RG, Pictor A.

Pictor A is a  $\gamma$ -ray emitting RG, located at a redshift of  $z = 0.035$  (Schmidt 1965). It has a bright primary hotspot, known as the western hotspot (WHS), which is situated about 4 arcmin ( $\sim 165$  kpc) away from the radio core (Perley et al. 1997). Its nucleus is a strong X-ray source and has been widely studied; a power-law (PL) spectrum is observed (Eracleous & Halpern 1998; Sambruna et al. 1999), maybe with a weak, narrow Fe  $K\alpha$  line (Hardcastle et al. 2016). Extensive research has also been conducted on this bright WHS (Roeser & Meisenheimer 1987; Thomson et al. 1995; Perley et al. 1997; Tingay et al. 2008; Simkin et al. 1999; Wilson et al. 2001; Isobe et al. 2017; Sunada et al. 2022; Thimmappa et al. 2022; Gulati et al. 2023; Shaik et al. 2024). The observed flat spectrum and flux variability in the X-ray band suggest that the X-rays from WHS are produced by

synchrotron radiation (Thimmappa et al. 2020; Sunada et al. 2022; Gulati et al. 2023; Shaik et al. 2024). X-ray polarization observations can serve as a valuable tool to verify its radiation mechanisms.

The  $\gamma$ -rays detected by Fermi-LAT for Pictor A are generally attributed to the contribution of the nucleus; adding the X-ray emission from the nucleus, they are produced through the synchrotron-self-Compton (SSC) process (Brown & Adams 2012; Xue et al. 2017; Gulati et al. 2023). However, it is also possible that the  $\gamma$ -rays stem from the WHS (Zhang et al. 2009). In this paper, we perform a comprehensive analysis of the  $\sim 16$ -year Fermi-LAT observation data to investigate the origins of  $\gamma$ -ray emission from Pictor A, and we examine the X-ray emission mechanisms of the nucleus and WHS using the IXPE observations for Pictor A in conjunction with the broadband SED modeling. Observations and data analysis are given in Section 2, followed by the presentation of results in Section 3. The SEDs of the nucleus and WHS are constructed and modeled in Section 4. A discussion and conclusions are presented in Section 5.  $H_0 = 71$  km s $^{-1}$  Mpc $^{-1}$ ,  $\Omega_m = 0.27$ , and  $\Omega_\Lambda = 0.73$  are adopted in this paper.

## 2. OBSERVATIONS AND DATA ANALYSIS

### 2.1. *Fermi-LAT*

Pictor A is associated with  $\gamma$ -ray source 4FGL J0519.6-4544 in the 4FGL-DR4 (Abdollahi et al. 2022; Ballet et al. 2023). We select the data within 15 $^\circ$  region of interest (ROI) centered on the radio position of Pictor A (R.A.=79 $^\circ$ .957, Decl.=−45 $^\circ$ .779) and download the PASS 8 data covering from 2008 August 4 to 2024 July 10 (MJD 54682–60501) within the energy range of 0.1–500 GeV from the Fermi Science Support Center<sup>1</sup>.

The publicly available software `fermitools` (v.2.2.0) and `Fermipy` (v.1.1; Wood et al. 2017) are used in our analysis. We use event class “SOURCE” (evclass=128) and event type “FRONT+BACK” (evtype=3) for the binned likelihood analysis based on LAT data selection recommendations<sup>2</sup> and set the maximum zenith angle of 90 $^\circ$  in order to eliminate the contamination of  $\gamma$ -ray emission from the earth limb. A standard filter expression “(DATA\_QUAL>0)&&(LAT\_CONFIG==1)” and the instrument response function of P8R3\_SOURCE\_V3 are used in our analysis. All of the  $\gamma$ -ray source models included in the 4FGL-DR4 (Abdollahi et al. 2020) within the ROI and two

<sup>1</sup> <https://fermi.gsfc.nasa.gov/cgi-bin/ssc/LAT/LATDataQuery.cgi>

<sup>2</sup> [https://fermi.gsfc.nasa.gov/ssc/data/analysis/documentation/Cicerone/Cicerone\\_Data\\_Exploration/Data\\_preparation.html](https://fermi.gsfc.nasa.gov/ssc/data/analysis/documentation/Cicerone/Cicerone_Data_Exploration/Data_preparation.html)

background model including the isotropic emission ("iso\_P8R3\_SOURCE\_V3\_V1.txt") and the diffuse galactic interstellar emission ("gll\_iem\_v07.fits") are added to the model. Only the parameters of the sources within  $6.5^\circ$  centered on Pictor A and the normalization of two background models are left free.

We use the test statistic (TS) to evaluate the significance of a  $\gamma$ -ray source signal,  $TS = 2(\log\mathcal{L}_{\text{src}} - \log\mathcal{L}_{\text{null}})$ , where  $\mathcal{L}_{\text{src}}$  and  $\mathcal{L}_{\text{null}}$  are the likelihood values of the background with and without the target source, respectively. The TS map of the Pictor A region is shown in the left panel of Figure 1, where the grey cross represents the best-fit position of the  $\gamma$ -ray source in this work, i.e., R.A. =  $79.91^\circ \pm 0.02^\circ$  and Decl. =  $-45.77^\circ \pm 0.02^\circ$ . This best-fit position is consistent with that of 4FGL J0519.6–4544 and spatially associated with Pictor A. As shown in the right panel of Figure 1, the maximum TS value of the residual TS map is  $\sim 4$ , indicating that the  $\gamma$ -ray emission from this source is well fitted by the model and no new  $\gamma$ -ray source is found. It should be noted that a bright flat-spectrum radio quasar (FSRQ), PKS J0515–4556, associated with 4FGL J0515.6–4556, is located  $0.75^\circ$  away from Pictor A. We have performed an extensive series of tests and conclusively ruled out any potential signal contamination from PKS J0515–4556. Further details are provided in Section 3.2.

The spectrum of Pictor A exhibits a broken power-law (BPL) shape, as shown in Figure 2. However, Pictor A is identified as a point-like source with a PL spectrum in 4FGL-DR4 (Abdollahi et al. 2022; Ballet et al. 2023). In order to evaluate which function provides a more accurate representation of the spectrum, We calculate the value of  $\Delta\text{TS}$ .  $\Delta\text{TS}$  is identified as

$$\Delta\text{TS} = 2(\log\mathcal{L}_{\text{BPL}} - \log\mathcal{L}_{\text{PL}}), \quad (1)$$

where  $\mathcal{L}_{\text{BPL}}$  and  $\mathcal{L}_{\text{PL}}$  are the obtained likelihood values utilizing BPL and PL functions, respectively. The PL function is defined as

$$\frac{dN(E)}{dE} = N_0 \times \left(\frac{E}{E_0}\right)^{-\Gamma_\gamma}, \quad (2)$$

and the BPL function is defined as

$$\frac{dN(E)}{dE} = N_0 \times \begin{cases} \left(\frac{E}{E_b}\right)^{-\Gamma_{\gamma,1}} & E < E_b \\ \left(\frac{E}{E_b}\right)^{-\Gamma_{\gamma,2}} & E \geq E_b \end{cases}, \quad (3)$$

where  $E_b$  represents the break energy,  $\Gamma_{\gamma,1}$  and  $\Gamma_{\gamma,2}$  are the indices below and above the break energy, respectively.

The  $\sim 16$ -year light curves in different energy bands are generated by freeing the normalizations of Pictor A

and 4FGL J0515.6–4556, while keeping all other spectral parameters fixed at their best-fit values obtained from the  $\sim 16$ -year data analysis. A likelihood-based statistic is the predominant approach for quantifying variability (Nolan et al. 2012; Peng et al. 2019; Abdollahi et al. 2020). To assess the variability of Pictor A, we adhere to the definition provided in Nolan et al. (2012) and calculate the variability index ( $\text{TS}_{\text{var}}$ ) as

$$\text{TS}_{\text{var}} = 2 \sum_{i=0}^N [\log(\mathcal{L}_i(F_i)) - \log(\mathcal{L}_i(F_{\text{glob}}))], \quad (4)$$

where  $N$  is the number of time bins,  $F_i$  is the fitting flux for bin  $i$ ,  $\mathcal{L}_i(F_i)$  is the likelihood corresponding to bin  $i$ , and  $F_{\text{glob}}$  is the best fit flux for the glob time by assuming a constant flux.

## 2.2. IXPE

Pictor A was observed by IXPE in two different periods: first from 2024 June 15 to 2024 July 5 with a total exposure of  $\sim 960$  ks (Obs.1), and second from 2024 November 13 to 2024 December 18 with a total exposure of  $\sim 934$  ks (Obs.2). The WHS is the primary target of these IXPE observations. However, the nucleus of Pictor A was also captured within the field of view (FOV) of IXPE, albeit in close proximity to the edge of the FOV.

The nucleus and WHS are both identified as point-like sources under a  $\sim 30''$  angular resolution of IXPE. Prior to conducting the IXPE data analysis, several corrections need to be applied to the publicly available Level-2 event files. Firstly, coordinate corrections are implemented to address detector pointing misalignment. Additionally, instrumental background is filtered using the `filter_background.py` script<sup>3</sup> to enhance the significance of results for faint sources with extended features (Di Marco et al. 2023). Given the long exposure time, good time intervals are filtered to mitigate particle events caused by solar activity (Ferrazzoli et al. 2024; Xie et al. 2024).

We calculate the X-ray polarization parameters from the IXPE observations using two different methods: (1) a model-independent method (Kislat et al. 2015); and (2) a spectropolarimetric analysis, as described in Strohmayer (2017). The source region of the nucleus is defined as a circle with a radius of  $60''$  centered on its radio position. Similarly, the source region for the WHS is also defined as a circle on the Chandra pointing position in Wilson et al. (2001), but with a smaller radius of

<sup>3</sup> <https://heasarc.gsfc.nasa.gov/docs/ixpe/analysis/contributed.html>

30'' due to its faintness compared to the nucleus. The background photons for both the nucleus and WHS are extracted from nearby circular regions with radii of 90'' and 45'', respectively, taking into account the effects of the FOV edges.

We first estimate the X-ray polarization of Pictor A for Obs.1 and Obs.2 separately; however, no significant differences are observed between these two observation periods. Therefore, to enhance photon statistics, we combine the data from Obs.1 and Obs.2 to estimate the polarization for both the nucleus and the WHS.

The polarization parameters of the nucleus and WHS are first calculated using the PCUBE algorithm within the `xpbin` task of the software `ixpeobssim` (v.31.0.3; Baldini et al. 2022) in the 2–8 keV energy range with the unweighted analysis method<sup>4</sup>. The influence of the sky background is eliminated following the background subtraction procedure presented in Baldini et al. (2022).

The spectropolarimetric analysis is performed using `Xspec` (v.12.14.1; Arnaud et al. 1999) in the HEASoft (v.6.34) package. Stokes parameter spectra ( $I$ ,  $Q$  and  $U$ ) for both the source and background are generated using the PHA1, PHA1Q, and PHA1U algorithms within `xpbin`. The  $I$ ,  $Q$  and  $U$  spectra are regrouped with a constant energy binning of 0.2 keV via the `ftgrouppha` task. Specifically, we utilize a weighted analysis method<sup>5</sup> on the  $I$ ,  $Q$  and  $U$  spectra to enhance the significance of the measurements using the `alpha075` response matrices. The spectropolarimetric fits are performed in a two-step procedure (e.g., Errando et al. 2024; Xie et al. 2024; Hu et al. 2024). Firstly, the  $I$  spectra are fitted with an absorbed PL model of the form  $\text{CONSTANT} \times \text{TBABS} \times \text{POWERLAW}$ . The PL function is

$$\frac{dN(E)}{dE} = N_0 \times \left( \frac{E}{E_0} \right)^{-\Gamma_X}, \quad (5)$$

where  $E_0 = 1$  keV is the scale parameter of photon energy,  $N_0$  is the PL normalization, and  $\Gamma_X$  is the photon spectral index (Massaro et al. 2004). The `CONSTANT` and `TBABS` models account for the uncertainties in the absolute effective area of the three detector units (DUs) and Galactic photoelectric absorption, respectively. The column densities are fixed to the Galactic values, i.e.,  $N_{\text{H}} = 3.62 \times 10^{20}$  cm<sup>-2</sup> for the nucleus and  $N_{\text{H}} = 3.57 \times 10^{20}$  cm<sup>-2</sup> for the WHS (HI4PI Collaboration et al. 2016). During the fits of the  $I$  spectra, both  $N_0$  and  $\Gamma_X$  are allowed to vary. Secondly, we simul-

taneously fit the  $I$ ,  $Q$  and  $U$  spectra of three DUs using an absorbed PL model with a constant polarization of the form  $\text{CONSTANT} \times \text{TBABS} \times \text{POLCONST} \times \text{POWERLAW}$ . The polarization model `POLCONST` assumes constant polarization parameters within the operating energy range and has only two free parameters: the X-ray polarization degree ( $\Pi_X$ ) and angle ( $\psi_X$ ). For these spectropolarimetric fits, the values of  $N_0$  and  $\Gamma_X$  are fixed at their best-fit values obtained from the  $I$  spectra fitting, leaving only  $\Pi_X$  and  $\psi_X$  as free parameters.

The analysis using the PCUBE algorithm within software `ixpeobssim` can yield a minimum detectable polarization at the 99% confidence level ( $\text{MDP}_{99}$ ). If the estimated value of  $\Pi_X$  is lower than the corresponding  $\text{MDP}_{99}$ , we will determine the 99% confidence level upper limit using the `error` task within the `Xspec` software package, following the recommendation provided in the IXPE statistics guide document<sup>6</sup>.

### 3. RESULTS

#### 3.1. Complex $\gamma$ -ray Behaviors of Pictor A

By analyzing the  $\sim 16$ -year Fermi-LAT observation data for Pictor A, we obtain  $\text{TS} \sim 773.10$  and an average flux of  $(1.06 \pm 0.08) \times 10^{-11}$  erg cm<sup>-2</sup> s<sup>-1</sup> in the 0.1–500 GeV energy band. As illustrated in Figure 2, the average spectrum of Pictor A over the full time shows a noticeable break at  $2.46 \pm 0.09$  GeV, with the spectral index hardening from  $\Gamma_{\gamma,1} = 3.25 \pm 0.15$  to  $\Gamma_{\gamma,2} = 1.81 \pm 0.07$ . The BPL spectral model is preferred over the single PL spectral model for fitting this spectrum at a confidence level of  $6.2\sigma$  ( $\Delta\text{TS} = 38.88$ ). Moreover, both energy bands (0.1–2.46 GeV and 2.46–500 GeV) can be well described by a PL function, yielding photon spectral indices of  $3.12 \pm 0.06$  and  $1.97 \pm 0.18$ , respectively, which are consistent with those obtained from fitting the entire energy band using a BPL model. These results are summarized in Table 1. These findings suggest the presence of statistically significant hardening in the observed  $\gamma$ -ray spectrum of Pictor A, similar to what has been observed in the other two RGs: Cen A (Sahakyan et al. 2013; Brown et al. 2017) and M87 (Ait Benkhali et al. 2019). Such an ‘‘unusual’’ break could most naturally be explained by a superposition of different spectral components. In order to further investigate the properties of GeV emission from Pictor A, additional data analysis on Fermi-LAT observations is conducted and the main findings are summarized below.

- *The full energy light curve.* We construct the  $\sim 16$ -year Fermi-LAT light curve of Pictor A in the 0.1–

<sup>4</sup> `weights=False` and `irfname='ixpe:obssim20240701:v013'` being set within `xpbin`.

<sup>5</sup> `weights=True` and `irfname='ixpe:obssim20240701_alpha075:v013'` being set within `xpbin`.

<sup>6</sup> <https://heasarc.gsfc.nasa.gov/docs/ixpe/analysis/>

500 GeV band using a uniform time-bin size of 90 days, as shown in Figure 3(a). To quantify the variability of the  $\gamma$ -ray light curve, we compute the variability index using Equation 4, yielding  $TS_{\text{var}} = 2715.7$  with  $N = 64$ . Given  $N - 1 = 63$  degrees of freedom, a value of  $TS_{\text{var}} \geq 135.9$  is required to identify variable sources at a confidence level of  $5\sigma$ . So, the result indicates that the  $\gamma$ -ray light curve of Pictor A exhibits significant flux variations at a confidence level substantially exceeding  $5\sigma$ . Based on a comparison of these fluxes with the average value, we tentatively identify two periods (F1 and F3) as high-flux states and one period (F2) as a low-flux state for Pictor A, as illustrated in Figure 3(a).

- *The light curves below and above the spectral break.* To investigate the temporal characteristics of the two spectral components, we also construct the light curves in the 0.1–2.46 GeV band (below the spectral break) and the 2.46–500 GeV band (above the spectral break), as displayed in Figures 3(b) and 3(c). Given the presence of numerous upper-limit points in the 0.1–500 GeV band light curve (Figure 3(a)), we use an adaptive-binning method with a criterion of  $TS \geq 9$  for each time bin to derive the light curves in the two energy bands. The minimum time-bin size is set to 90 days, consistent with the time-bin size used for the 0.1–500 GeV light curve. Additionally, we compute the  $TS_{\text{var}}$  values for both light curves, obtaining  $TS_{\text{var}} = 2306.3$  with  $N = 28$  for the low-energy light curve (a value of  $TS_{\text{var}} \geq 80.8$  with  $N - 1 = 27$  degrees of freedom is required to identify variable sources at a confidence level of  $5\sigma$ ) and  $TS_{\text{var}} = 5.5$  with  $N = 7$  (corresponding to  $0.05\sigma$ ) for the high-energy light curve, respectively. Notably, the low-energy light curve demonstrates significant flux variability substantially exceeding a confidence level of  $5\sigma$ , whereas no significant flux variability is observed in the high-energy light curve. This indicates that the dominant statistical contribution to the full energy light curve comes from the low-energy band component. Detailed information for each time bin of the two light curves is provided in Table 2.
- *The spectra of low-flux and high-flux states.* The spectrum shown in Figure 2 is a  $\sim 16$ -year average spectrum, covering the different flux states of source. We thus extract the time-integrated spectra in the 0.1–500 GeV band for three different stages: MJD 55762–58732 (period F2) for the

low-flux state, together with MJD 54952–55762 (period F1) and MJD 58822–59272 (period F3) for the two high-flux states, respectively. Using Equation 1, we obtain  $\Delta TS = 0.63$  for the F1 state and  $\Delta TS = 1.55$  for the F3 state, respectively. These values suggest that the BPL spectral shape is not significant in either spectrum. As illustrated in Figure 2, both spectra from the high-flux states can be well fitted using a PL function. However, they exhibit different spectral indices:  $\Gamma_{\gamma} = 2.59 \pm 0.21$  for the F1 state and  $\Gamma_{\gamma} = 3.30 \pm 0.17$  for the F3 state. Nonetheless, to account for the low-flux spectrum (F2 state), a BPL function is still necessary ( $\Delta TS = 11.51$ , corresponding to a significance of  $3.4\sigma$ ), characterized by  $\Gamma_{\gamma,1} = 3.13 \pm 0.08$ ,  $\Gamma_{\gamma,2} = 1.92 \pm 0.16$ , and a break energy of  $2.15 \pm 0.27$  GeV.

The aforementioned findings provide support for the idea that the spectrum depicted in Figure 2 results from the superposition of two distinct physical components. One component dominates the low-energy band, particularly during periods of high-flux emission, while another component primarily contributes to the high-energy band, which is more prominent during low-flux state of the source. The contrasting variability patterns above and below the spectral break could potentially serve as additional evidence for the existence of these two separate components in the  $\gamma$ -ray emission of Pictor A.

### 3.2. Assessing the Contamination from 4FGL J0515.6–4556

To investigate whether the broken  $\gamma$ -ray spectrum of Pictor A is influenced by contamination from the radiation of 4FGL J0515.6–4556 (associated with the FSRQ PKS J0515–4556), we conduct a series of tests as follows.

- *Contributions of  $\gamma$ -rays above 2 GeV.* We first consider an extreme scenario wherein the observed  $\gamma$ -ray emission is attributed solely to 4FGL J0515.6–4556, by removing 4FGL J0519.6–4544 from the *model.xml*. As the angular resolution of the LAT is less than  $0.6^\circ$  at 2 GeV (Atwood et al. 2009), we generate a  $3^\circ \times 3^\circ$  residual TS map centered on the radio position of Pictor A by re-analyzing 16-year Fermi-LAT data in the 2.0–500 GeV band. As shown in the left panel of Figure 4, a significant residual signal with a maximum TS value of 67 is clearly observed at the location of Pictor A. Therefore, it is evident that the model considering only the single source 4FGL J0515.6–4556 cannot fully account for all observed emission. There are

substantial contributions of  $\gamma$ -rays above 2 GeV originating from Pictor A.

- *The spectra above 2.46 GeV.* As shown in Figure 2, the  $\gamma$ -ray spectrum of Pictor A displays a spectral break at 2.46 GeV. We thus re-analyze the 16-year Fermi-LAT data above 2.46 GeV (break energy) to simultaneously generate the spectra of Pictor A and PKS J0515–4556, as illustrated in Figure 5. Notably, Pictor A displays a flat power-law spectrum, while PKS J0515–4556 follows a log-parabolic spectral shape. The derived spectrum of PKS J0515–4556 is consistent with that reported in the 4FGL-DR4 (Abdollahi et al. 2022; Ballet et al. 2023). Furthermore, the flux of PKS J0515–4556 decreases logarithmically, becoming comparable to that of Pictor A around 30 GeV, while the  $\gamma$ -ray flux of Pictor A exhibits a gradual increase extending beyond 100 GeV.
- *TS map above 20 GeV.* To further investigate whether the high-energy emission in the energy band 20–500 GeV primarily originates from the bright PKS J0515–4556, we re-generate the TS map of Pictor A and PKS J0515–4556, as illustrated in the right panel of Figure 4. The maximum TS values obtained are 25 for Pictor A and 40 for PKS J0515–4556, respectively. Considering the angular resolution of the LAT above 20 GeV is much better than 0.75 degrees, these results indicate that Pictor A also contributes significantly to the high-energy  $\gamma$ -ray emission, which is consistent with our previous spectral analysis.

The results from the above analysis are consistent, indicating that the spectral break at 2.46 GeV observed in Pictor A is not attributable to contamination from emission by PKS J0515–4556. It should be noted that the systematic uncertainty associated with the Point Spread Function (PSF) was not incorporated into the analysis, as the Fermi team is still conducting an ongoing study of the LAT PSF using in-orbit data. Nevertheless, even considering the maximum uncertainty of the PSF within the energy band above 10 GeV, the PSF at 10 GeV expands only to  $0.19^\circ$  (with an uncertainty of 25% and a PSF value of  $0.15^\circ$ ). Given that the angular separation between the two sources is  $0.75^\circ$ , we conclude that this level of PSF uncertainty does not significantly affect the spectral results.

### 3.3. Possible $\gamma$ -ray Emission from WHS

The analysis results of the Fermi-LAT data clearly indicate that the  $\gamma$ -rays detected from Pictor A have

two distinct origins: one component dominates the observed flux and exhibits significant variability, primarily contributing to the emission at low energies (below the spectral break) with a steep spectrum; while another component contributes to the high-energy emission (above the spectral break) without evident variability, displaying a hard spectrum. Through broadband SED fitting of the nucleus and WHS in Pictor A, Zhang et al. (2009) proposed that there is detectable  $\gamma$ -ray emission in WHS. The combined spectrum from both the nucleus and WHS in the GeV band would manifest as a BPL feature, with a harder spectrum at higher energy ranges, as illustrated in Figure 3 of their study. Therefore, we suggest that the high-energy component observed above the spectral break in Pictor A is predominantly due to the emission from WHS, while radiation from the nucleus primarily accounts for low-energy emission below this break and exhibits evident variability in Pictor A.

### 3.4. X-Ray Polarization of the nucleus and WHS

The PCUBE analysis yields an  $\text{MDP}_{99}$  of 5.4% for the nucleus and an  $\text{MDP}_{99}$  exceeding 90% for the WHS, based on the combined data from the three IXPE DUs, as shown in Figure 6. No significant detection of X-ray polarization at a confidence level greater than 99% is observed in the 2–8 keV band for both the nucleus and the WHS. Due to the limited number of detected photons, the estimated  $\text{MDP}_{99}$  value for the WHS surpasses the theoretical maximum polarization degree of  $\sim 70\%$ . Based on the spectropolarimetric fitting results presented in Figure 7, upper limits for the polarization degree are derived:  $\Pi_X < 6.6\%$  for the nucleus and  $\Pi_X < 56.4\%$  for the WHS, at a 99% confidence level within the 2–8 keV band. Figure 8 illustrates the confidence levels of the measurements for both the nucleus and WHS through polarization contour plots. The detailed optimal parameters derived from the spectropolarimetric fitting are summarized in Table 3.

We also perform an energy-resolved polarization analysis on the nucleus following the methodology provided in Errando et al. (2024) and Hu et al. (2024). Specifically, we divide the entire 2–8 keV energy range into finer energy bins (1 keV, 1.5 keV, 2 keV, and 3 keV) and estimate the X-ray polarization parameters for each bin using both the model-independent approach and the spectropolarimetric method. As displayed in Figure 9, the polarization parameters can be estimated with a confidence level exceeding 99% only within the energy ranges of 4–6 keV and 5–6.5 keV using both the model-independent approach and the spectropolarimetric method. Based on the spectropolarimetric fit results,

we obtain  $\Pi_X = 9.5\% \pm 2.4\%$  with  $\psi_X = 107.0^\circ \pm 7.2^\circ$  in the 4–6 keV band at a confidence level of  $4.0\sigma$ , and  $\Pi_X = 13.8\% \pm 3.9\%$  with  $\psi_X = 119.7^\circ \pm 8.0^\circ$  in the 5–6.5 keV band at a confidence level of  $3.5\sigma$ . Meanwhile, the PCUBE analysis yields  $\Pi_X = 9.0\% \pm 2.6\%$  with  $\psi_X = 104.7^\circ \pm 8.4^\circ$  and  $\Pi_X = 14.2\% \pm 4.3\%$  with  $\psi = 126.7^\circ \pm 8.7^\circ$  for the respective energy bands. The derived values of  $\psi_X$  are slight larger than the jet position angle, which is approximately  $100^\circ$  (Perley et al. 1997; Tingay et al. 2000).

The radio (Perley et al. 1997) and optical bands (Roeser & Meisenheimer 1987; Thomson et al. 1995) have detected high polarization in WHS, reaching up to the theoretical maximum of approximately 70%. Furthermore, there is a remarkable similarity in structures between the radio and optical bands. Due to the limited number of detected photons, the IXPE observations for WHS do not yield significant polarization data. However, we can establish an upper limit on the polarization degree for WHS, i.e.,  $\Pi_X < 56.4\%$  at a 99% confidence level in the 2–8 keV band.

#### 4. CONSTRUCTING AND MODELING THE SED

The observed BPL spectral pattern in Pictor A, characterized by a harder spectrum at higher energy bands, suggests the existence of two distinct components contributing to its  $\gamma$ -ray emission. In order to further investigate the  $\gamma$ -ray emission characteristics of Pictor A, we construct broadband SEDs for both the nucleus and WHS regions, covering the energy band from radio to  $\gamma$ -rays, as illustrated in Figure 10. The data for both the nucleus and WHS, ranging from radio to X-rays, are obtained from Gulati et al. (2023) and references therein (for more details, please refer to the caption of Figure 10), while the  $\gamma$ -ray spectrum is derived through our own analysis in this study. As described in Section 3, the low-energy and high-energy components are proposed to primarily originate from the nucleus and WHS, respectively. The results appear to be consistent with their broadband SEDs, as shown in Figure 10; the combinations with their respective radio to X-ray data result in smooth features in their broadband SEDs.

The leptonic model is commonly used to fit the broadband SEDs of the jet emission from AGNs. The radiation region is assumed to be a sphere with a radius  $R$ , magnetic field strength  $B$ , the bulk Lorentz factor  $\Gamma$ , and the Doppler boosting factor  $\delta$ . The electron distribution in the emission region is taken as a PL or a BPL, characterized by an electron density parameter ( $N_0$ ), a break energy ( $\gamma_b$ ), and indices ( $p_1$  and  $p_2$ ) ranging from  $\gamma_{\min}$  to  $\gamma_{\max}$ . In the case of a PL electron distribution,  $p_1 = p_2$  and  $\gamma_b = \gamma_{\max}$ . Additionally, the synchrotron-

self absorption, Klein–Nishina effect, and extragalactic background light absorption (Finke et al. 2022) are considered during the SED modeling.

##### 4.1. Nucleus Region

The synchrotron and SSC processes of relativistic electrons with a BPL distribution are commonly used to explain the observed SED of the nucleus in  $\gamma$ -ray emitting RGs (Abdo et al. 2009; Migliori et al. 2011; Fukazawa et al. 2015; Xue et al. 2017; Yu et al. 2024), which is also used to represent the observed SED of the nucleus in Pictor A. The emission region radius is fixed at  $R = 10^{16}$  cm, as also mentioned in Zhang et al. (2009) and Gulati et al. (2023). We adopt  $\Gamma = 5$  with a viewing angle of  $30^\circ$  (Gulati et al. 2023), corresponding to  $\delta = 1.3$ . The values of  $p_1$  and  $p_2$  are determined using the observed spectral indices in X-rays and optical–UV bands, respectively. We set  $\gamma_{\min} = 1$ , while  $\gamma_{\max}$  is approximately constrained by the observed GeV spectrum, showing a cutoff at the break frequency. By adjusting the parameters  $B$ ,  $N_0$ , and  $\gamma_b$  to match the broadband SED of the nucleus, we obtain  $B = 7$  G,  $\gamma_b = 1.6 \times 10^3$ , and  $\gamma_{\max} = 1.6 \times 10^4$ . The modeling parameters are also listed in Table 4.

The fitting result is presented in Figure 10; the one-zone synchrotron+SSC model well represents the broadband SED of the nucleus. It is evident that this model fails to account for the high-energy component observed in the Fermi-LAT spectrum, even without considering the low-energy component of the  $\gamma$ -ray spectrum. If the high-energy component also stems from the inner jet of Pictor A, a more complex radiation model is required to reproduce the observed broadband SED of nucleus, such as a spine-layer model (Tavecchio & Ghisellini 2008) or hadronic processes (e.g., Cheng et al. 2022).

It should be noted that the derived parameter values are based on visual assessments, resulting in a set of model parameters that provide an acceptable fit. Furthermore, there exists a degeneracy between  $B$  and  $\delta$  during the SED modeling process (e.g., Zhang et al. 2012). For instance, with a similar value of  $R \sim 10^{16}$  cm, Gulati et al. (2023) reported  $\delta = 1.3$  with  $B = 10$  G, whereas Zhang et al. (2009) found  $\delta = 1.6$  with  $B = 7$  G, and Xue et al. (2017) obtained  $\delta = 2.5$  with  $B = 4.2$  G. Considering the dominance of the low-energy component in the high-flux  $\gamma$ -ray emission state of Pictor A, as illustrated in Figure 2, we incorporate the X-ray spectrum obtained during the high-flux state (Gulati et al. 2023) into account in our SED modeling. Consequently, the obtained value of  $B$  differs from theirs due to the different X-ray and  $\gamma$ -ray data.

#### 4.2. WHS

Considering the complex radio structure (Perley et al. 1997; Tingay et al. 2008) and flat X-ray spectrum of WHS (e.g., Zhang et al. 2009; Gulati et al. 2023), we use a two-zone leptonic model to fit its broadband SED from radio to X-rays, same model as taken in Zhang et al. (2009) and Gulati et al. (2023). This model includes synchrotron and SSC radiations originating from both a diffuse region and a compact substructure, where both regions are treated as stationary blobs characterized by  $\Gamma = \delta = 1$ . The energy density of the synchrotron radiation field in this scenario surpasses that of the cosmic microwave background (CMB) by more than one order of magnitude. Consequently, the contribution of the IC scattering of CMB photons by relativistic electrons can be considered negligible when compared to the SSC process. The emission of WHS from radio, optical to ultraviolet is primarily attributed to the synchrotron process occurring in the whole diffuse region, while the X-rays are produced through synchrotron radiation emitted by a compact substructure contained within the diffuse region. The  $\gamma$ -ray spectrum above the break in Figure 2 is taken into consideration in the SED modeling of the WHS.

For the diffuse region of WHS, a radius of  $R = 500$  pc is adopted, which corresponds to half of the overall size (1.4 arcsec, Thomson et al. 1995) of WHS in the optical band. The electron distribution follows a BPL, with  $p_1$  and  $p_2$  being well constrained by observed data across radio to UV bands.  $\gamma_{\min}$  cannot be determined and is fixed at 1, while  $\gamma_{\max}$  is roughly constrained by the last data point in the UV band. Considering the equipartition condition ( $U_B = U_e$ ), where  $U_B$  and  $U_e$  are the energy densities of the magnetic fields and electrons in the radiation region, it is found that the prediction flux from SSC process fails to explain the  $\gamma$ -ray spectrum at GeV energies. The fitting of the highest-energy point in the GeV band necessitates a significantly small magnetic field that deviates substantially from the equipartition condition, while also resulting in the model's prediction line surpassing the two data points above the break. Therefore, we abandon this hypothesis.

For the compact substructure of WHS, a radius of  $R = 30$  pc is taken, which is half the average size of the five compact substructures reported by Tingay et al. (2008). Considering the limited observational data, we adopt a PL electron distribution.  $p_1$  is determined based on the spectral index between radio and soft X-rays.  $\gamma_{\min}$  is also fixed at 1. When considering equipartition conditions, the predicted line from the SSC process is significantly lower than the  $\gamma$ -ray fluxes observed at the GeV band, similar to that of the diffuse region. We pro-

pose that the  $\gamma$ -rays primarily originate from the compact substructure; therefore, the equipartition condition in the compact substructure is not taken into account during SED modeling of WHS.

We adjust the values of  $N_0$  and  $\gamma_b$  for the diffuse region under the equipartition condition, along with adjusting the parameters  $N_0$ ,  $B$ , and  $\gamma_{\max}$  of the compact substructure to represent the observed SED of WHS from radio to  $\gamma$ -ray bands. The fitting parameter values are visually assessed and are provided in Table 4. The fitting result is presented in Figure 10. The parameter values for the diffuse region are found to be comparable to those reported in Gulati et al. (2023). However, the  $B$  value for the compact substructure is one order of magnitude smaller, accompanied by a slightly higher value of  $\gamma_{\max}$  in order to match the  $\gamma$ -ray spectrum. Additionally, we observe that the predicted flux of SED modeling is over the sensitivity curve of Cherenkov Telescope Array (CTA) south array (CTA-S, 50 hr), but remains below the sensitivity of High Energy Stereoscopic System (H.E.S.S.), where the sensitivity curves are obtained from Wang et al. (2022) and the CTA webpage<sup>7</sup>, respectively. Considering the hard spectrum in the GeV band, it could potentially be considered as a candidate for CTA.

#### 5. DISCUSSION AND CONCLUSIONS

By analyzing the Fermi-LAT observation data, we find that the  $\sim 16$ -year average spectrum of Pictor A in the GeV band exhibits statistically significant hardening feature. The BPL spectral form is more preferred than a simple PL function for describing the  $\gamma$ -ray spectrum of Pictor A with a confidence level of  $6.2\sigma$ . Pictor A was initially identified as a  $\gamma$ -ray source by Brown & Adams (2012) using the first three years of Fermi-LAT data. Subsequently, Angioni et al. (2019) analyzed  $\sim 8.5$  years of Fermi-LAT data in the 0.1–100 GeV energy range for Pictor A, while Rulten et al. (2020) examined  $\sim 10$  years of Fermi-LAT observations spanning 0.1–300 GeV. Both studies reported a single PL spectrum for Pictor A with photon spectral indices  $\Gamma_\gamma = 2.63 \pm 0.08$  and  $\Gamma_\gamma = 2.37 \pm 0.10$ , respectively. Notably, Rulten et al. (2020) also reported the detection of a photon with an energy exceeding 100 GeV (in their figure 3). To quantitatively evaluate the impact of energy range and exposure time on the spectral break, we calculate the difference in TS values ( $\Delta$ TS) between PL model and BPL model (as described in Section 3.1) for different observation durations. For the first 8.5-year dataset, consistent

<sup>7</sup> <https://www.ctao.org/for-scientists/performance/>

with the duration in Angioni et al. (2019), the  $\Delta TS$  values are 1.23 (corresponding to  $1.1\sigma$ ) in the 0.1–100 GeV energy band and 6.85 ( $2.6\sigma$ ) when extending to 0.1–500 GeV (Figure 5). Within the full 16-year dataset, these values significantly increase to 20.17 ( $4.5\sigma$ ) in the 0.1–100 GeV energy band and 38.88 ( $6.2\sigma$ ) in the broader 0.1–500 GeV energy band. This progressive enhancement of significance demonstrates that increasing the exposure time improves the spectral break detection significance across all energy bands, while expanding the energy range to 500 GeV further enhances the statistical robustness of high-energy spectral features.

Significant spectral hardening behavior in the GeV  $\gamma$ -ray band has also been observed in two other RGs: Cen A (Sahakyan et al. 2013; Brown et al. 2017) and M 87 (Ait Benkhali et al. 2019). In both cases, it was proposed that the GeV emission consists of two distinct physical components. For M 87, the hardening  $\gamma$ -ray spectrum was observed at a significance level of  $\sim 2.66\sigma$ , and both components were suggested to stem from the inner jet (Ait Benkhali et al. 2019). For Cen A, the significance level of the hardening  $\gamma$ -ray spectrum increased from  $2.3\sigma$  (Sahakyan et al. 2013) based on the 4-year Fermi-LAT observation data to  $> 5\sigma$  (Brown et al. 2017) when utilizing the 8-year Fermi-LAT observation data. They suggested that this additional high-energy component beyond the common SSC emission may be related with the interactions between relativistic protons and ambient gas in the large-scale jet (Sahakyan et al. 2013), or the dark matter around the black hole, or a population of millisecond pulsars in the core region (Brown et al. 2017).

The low-energy component, characterized by a steep spectrum and significant variability, is likely to originate from the nucleus and accounts for the majority of the emission flux of Pictor A. Contrarily, the high-energy component, which exhibits a hard spectrum and remains in a steady emission state, is favored by the extended  $\gamma$ -ray production scenario. We propose that this high-energy component stems from the WHS, and that the observed BPL spectrum in the GeV band of Pictor A results from the combined emission originating from both its nucleus and WHS.

We use a single-zone leptonic model to explain the broadband SED of the nucleus, while adopting a two-zone leptonic model to represent the broadband SED of WHS. The two components in the GeV spectrum of Pictor A smoothly connect with the X-ray spectra of the nucleus and WHS, respectively; both can be naturally represented by the SSC process occurring in two different regions. Moreover, our SED fitting predicts that CTA-S will be able to detect very high-energy (VHE) emis-

sion from WHS. Notably, H.E.S.S. observations have unveiled VHE  $\gamma$ -ray emission along the large-scale jet of RG Cen A (H. E. S. S. Collaboration et al. 2020), providing compelling evidence supporting large-scale jets as sites for accelerating ultrarelativistic electrons.

By analyzing the IXPE observational data for Pictor A, we have derived an upper limit of  $\Pi_X < 6.6\%$  for the polarization degree in the 2–8 keV band of the nucleus at a 99% confidence level. This finding is consistent with the low-polarization expectation that the X-ray emission of the nucleus is produced by the SSC process (Krawczynski 2012; Peirson & Romani 2019), similar to the IXPE observation results of RG Cen A (Ehlert et al. 2022) and other low and intermediate spectral peak blazars (Marshall et al. 2023). We also note that the nucleus of Pictor A generally exhibits low polarization in the radio band, typically less than 5% (Perley et al. 1997 and references therein). However, no optical polarimetry data is available in the archived records.

While no significant polarization is detected in the 2–8 keV band for the nucleus, X-ray polarization signals are detected in several narrow energy bins with a confidence level exceeding 99%, as illustrated in Figure 9. As described in Section 2.2, the X-ray spectrum of the nucleus can be adequately explained by a simple PL function. This is also consistent with recent studies employing other X-ray detectors (e.g., Sunada et al. 2022; Gulati et al. 2023). It is unlikely that this narrow-energy-band polarization arises from superimposed components originating from other regions or radiation processes. Given that the detection significance in these narrow energy bins is  $\leq 4\sigma$ , we propose this to be a tentative detection, which may potentially be attributed to statistical fluctuations.

Numerous studies have suggested that the X-rays emitted by WHS originate from synchrotron radiation within a compact substructure (Wilson et al. 2001; Tingay et al. 2008; Zhang et al. 2009; Hardcastle et al. 2016; Gulati et al. 2023). Considering the significant polarization observed in both radio and optical bands, with some measurements reaching up to the theoretical maximum of approximately 70% (Roeser & Meisenheimer 1987; Thomson et al. 1995; Perley et al. 1997), it is expected that high polarization detection of WHS in the X-ray band would provide a valuable tool for investigating radiation mechanisms of X-rays in WHS. Unfortunately, due to the limited number of detected photons in the IXPE observations, we have only been able to establish an upper limit of  $\Pi_X < 56.4\%$  at a 99% confidence level within the 2–8 keV band, which does not provide sufficient information to further examine the X-ray emission mechanism in WHS.

1 We sincerely appreciate the referee for the valuable  
2 suggestions, which have greatly enhanced the quality of  
3 the manuscript. We also appreciate helpful discussion  
4 with Fei Xie. This work reports observations obtained  
5 with the Imaging X-ray Polarimetry Explorer (IXPE),  
6 a joint US (NASA) and Italian (ASI) mission, led by  
7 Marshall Space Flight Center (MSFC). The research  
8 uses data products provided by the IXPE Science Op-  
9 erations Center (MSFC), using algorithms developed by  
10 the IXPE Collaboration, and distributed by the High-  
11 Energy Astrophysics Science Archive Research Center  
12 (HEASARC). This work is supported by the National  
13 Key R&D Program of China (grant 2023YFE0117200)  
14 and the National Natural Science Foundation of China  
15 (grants 12203022, 12022305, 11973050, and 12373041).

## REFERENCES

- Abdo, A. A., Ackermann, M., Ajello, M., et al. 2009, *ApJ*, 707, 55, doi: [10.1088/0004-637X/707/1/55](https://doi.org/10.1088/0004-637X/707/1/55)
- . 2010, *ApJ*, 719, 1433, doi: [10.1088/0004-637X/719/2/1433](https://doi.org/10.1088/0004-637X/719/2/1433)
- Abdollahi, S., Acero, F., Ackermann, M., et al. 2020, *ApJS*, 247, 33, doi: [10.3847/1538-4365/ab6bcb](https://doi.org/10.3847/1538-4365/ab6bcb)
- Abdollahi, S., Acero, F., Baldini, L., et al. 2022, *ApJS*, 260, 53, doi: [10.3847/1538-4365/ac6751](https://doi.org/10.3847/1538-4365/ac6751)
- Ackermann, M., Ajello, M., Baldini, L., et al. 2016, *ApJ*, 826, 1, doi: [10.3847/0004-637X/826/1/1](https://doi.org/10.3847/0004-637X/826/1/1)
- Ait Benkhali, F., Chakraborty, N., & Rieger, F. M. 2019, *A&A*, 623, A2, doi: [10.1051/0004-6361/201732334](https://doi.org/10.1051/0004-6361/201732334)
- Angioni, R., Ros, E., Kadler, M., et al. 2019, *A&A*, 627, A148, doi: [10.1051/0004-6361/201935697](https://doi.org/10.1051/0004-6361/201935697)
- Arnaud, K., Dorman, B., & Gordon, C. 1999, XSPEC: An X-ray spectral fitting package, *Astrophysics Source Code Library*, record ascl:9910.005. <http://ascl.net/9910.005>
- Atwood, W. B., Abdo, A. A., Ackermann, M., et al. 2009, *ApJ*, 697, 1071, doi: [10.1088/0004-637X/697/2/1071](https://doi.org/10.1088/0004-637X/697/2/1071)
- Baldini, L., Bucciantini, N., Lalla, N. D., et al. 2022, *SoftwareX*, 19, 101194, doi: [10.1016/j.softx.2022.101194](https://doi.org/10.1016/j.softx.2022.101194)
- Ballet, J., Bruel, P., Burnett, T. H., Lott, B., & The Fermi-LAT collaboration. 2023, arXiv e-prints, arXiv:2307.12546, doi: [10.48550/arXiv.2307.12546](https://doi.org/10.48550/arXiv.2307.12546)
- Brown, A. M., & Adams, J. 2012, *MNRAS*, 421, 2303, doi: [10.1111/j.1365-2966.2012.20451.x](https://doi.org/10.1111/j.1365-2966.2012.20451.x)
- Brown, A. M., BÅ'hm, C., Graham, J., et al. 2017, *PhRvD*, 95, 063018, doi: [10.1103/PhysRevD.95.063018](https://doi.org/10.1103/PhysRevD.95.063018)
- Cheng, J.-G., Huang, X.-L., Wang, Z.-R., Huang, J.-K., & Liang, E.-W. 2022, *ApJL*, 925, L19, doi: [10.3847/2041-8213/ac4d8e](https://doi.org/10.3847/2041-8213/ac4d8e)
- Cutri, R. M., Wright, E. L., Conrow, T., et al. 2013, Explanatory Supplement to the AllWISE Data Release Products, Explanatory Supplement to the AllWISE Data Release Products, by R. M. Cutri et al.
- Di Gesu, L., Donnarumma, I., Tavecchio, F., et al. 2022, *ApJL*, 938, L7, doi: [10.3847/2041-8213/ac913a](https://doi.org/10.3847/2041-8213/ac913a)
- Di Marco, A., Soffitta, P., Costa, E., et al. 2023, *AJ*, 165, 143, doi: [10.3847/1538-3881/acba0f](https://doi.org/10.3847/1538-3881/acba0f)
- Ehlert, S. R., Ferrazzoli, R., Marinucci, A., et al. 2022, *ApJ*, 935, 116, doi: [10.3847/1538-4357/ac8056](https://doi.org/10.3847/1538-4357/ac8056)
- Ehlert, S. R., Liodakis, I., Middei, R., et al. 2023, *ApJ*, 959, 61, doi: [10.3847/1538-4357/ad05c4](https://doi.org/10.3847/1538-4357/ad05c4)
- Eracleous, M., & Halpern, J. P. 1998, *ApJ*, 505, 577, doi: [10.1086/306190](https://doi.org/10.1086/306190)
- Errando, M., Liodakis, I., Marscher, A. P., et al. 2024, *ApJ*, 963, 5, doi: [10.3847/1538-4357/ad1ce4](https://doi.org/10.3847/1538-4357/ad1ce4)
- Ferrazzoli, R., Prokhorov, D., Bucciantini, N., et al. 2024, *ApJL*, 967, L38, doi: [10.3847/2041-8213/ad4a68](https://doi.org/10.3847/2041-8213/ad4a68)
- Finke, J. D., Ajello, M., Domínguez, A., et al. 2022, *ApJ*, 941, 33, doi: [10.3847/1538-4357/ac9843](https://doi.org/10.3847/1538-4357/ac9843)
- Fukazawa, Y., Finke, J., Stawarz, L., et al. 2015, *ApJ*, 798, 74, doi: [10.1088/0004-637X/798/2/74](https://doi.org/10.1088/0004-637X/798/2/74)
- Georganopoulos, M., & Kazanas, D. 2003, *The Astrophysical Journal*, 589, L5–L8, doi: [10.1086/375796](https://doi.org/10.1086/375796)
- Gulati, S., Bhattacharya, D., Ramadevi, M. C., Stalin, C. S., & Sreekumar, P. 2023, *MNRAS*, 521, 2704, doi: [10.1093/mnras/stad716](https://doi.org/10.1093/mnras/stad716)
- Guo, S.-C., Zhang, H.-M., Zhang, J., & Liang, E.-W. 2018, *Research in Astronomy and Astrophysics*, 18, 070, doi: [10.1088/1674-4527/18/6/70](https://doi.org/10.1088/1674-4527/18/6/70)
- H. E. S. S. Collaboration, Abdalla, H., Adam, R., et al. 2020, *Nature*, 582, 356, doi: [10.1038/s41586-020-2354-1](https://doi.org/10.1038/s41586-020-2354-1)
- Hardcastle, M. J., Lenc, E., Birkinshaw, M., et al. 2016, *MNRAS*, 455, 3526, doi: [10.1093/mnras/stv2553](https://doi.org/10.1093/mnras/stv2553)
- Harris, D. E., & Krawczynski, H. 2006, *ARA&A*, 44, 463, doi: [10.1146/annurev.astro.44.051905.092446](https://doi.org/10.1146/annurev.astro.44.051905.092446)
- He, J.-C., Sun, X.-N., Wang, J.-S., et al. 2023, *MNRAS*, 525, 5298, doi: [10.1093/mnras/stad2542](https://doi.org/10.1093/mnras/stad2542)
- HI4PI Collaboration, Ben Bekhti, N., Flöer, L., et al. 2016, *A&A*, 594, A116, doi: [10.1051/0004-6361/201629178](https://doi.org/10.1051/0004-6361/201629178)
- Hu, X.-K., Yu, Y.-W., Zhang, J., et al. 2024, *ApJL*, 970, L22, doi: [10.3847/2041-8213/ad5e68](https://doi.org/10.3847/2041-8213/ad5e68)
- Isobe, N., Koyama, S., Kino, M., et al. 2017, *ApJ*, 850, 193, doi: [10.3847/1538-4357/aa94c9](https://doi.org/10.3847/1538-4357/aa94c9)
- Isobe, N., Sunada, Y., Kino, M., et al. 2020, *ApJ*, 899, 17, doi: [10.3847/1538-4357/ab9d1c](https://doi.org/10.3847/1538-4357/ab9d1c)
- Kataoka, J., & Stawarz, L. 2005, *ApJ*, 622, 797, doi: [10.1086/428083](https://doi.org/10.1086/428083)
- Kislat, F., Clark, B., Beilicke, M., & Krawczynski, H. 2015, *Astroparticle Physics*, 68, 45, doi: [10.1016/j.astropartphys.2015.02.007](https://doi.org/10.1016/j.astropartphys.2015.02.007)
- Kouch, P. M., Liodakis, I., Middei, R., et al. 2024, *A&A*, 689, A119, doi: [10.1051/0004-6361/202449166](https://doi.org/10.1051/0004-6361/202449166)
- Krawczynski, H. 2012, *ApJ*, 744, 30, doi: [10.1088/0004-637X/744/1/30](https://doi.org/10.1088/0004-637X/744/1/30)
- Liodakis, I., Marscher, A. P., Agudo, I., et al. 2022, *Nature*, 611, 677, doi: [10.1038/s41586-022-05338-0](https://doi.org/10.1038/s41586-022-05338-0)
- Marshall, H. L., Liodakis, I., Marscher, A. P., et al. 2023, arXiv e-prints, arXiv:2310.11510, doi: [10.48550/arXiv.2310.11510](https://doi.org/10.48550/arXiv.2310.11510)
- . 2024, *ApJ*, 972, 74, doi: [10.3847/1538-4357/ad5671](https://doi.org/10.3847/1538-4357/ad5671)
- Massaro, E., Perri, M., Giommi, P., & Nesci, R. 2004, *A&A*, 413, 489, doi: [10.1051/0004-6361:20031558](https://doi.org/10.1051/0004-6361:20031558)
- Meisenheimer, K., Roser, H. J., Hiltner, P. R., et al. 1989, *A&A*, 219, 63
- Meisenheimer, K., Yates, M. G., & Roeser, H. J. 1997, *A&A*, 325, 57

- Middei, R., Liodakis, I., Perri, M., et al. 2023a, *ApJL*, 942, L10, doi: [10.3847/2041-8213/aca281](https://doi.org/10.3847/2041-8213/aca281)
- Middei, R., Perri, M., Puccetti, S., et al. 2023b, *ApJL*, 953, L28, doi: [10.3847/2041-8213/acec3e](https://doi.org/10.3847/2041-8213/acec3e)
- Migliori, G., Grandi, P., Torresi, E., et al. 2011, *A&A*, 533, A72, doi: [10.1051/0004-6361/201116808](https://doi.org/10.1051/0004-6361/201116808)
- Nolan, P. L., Abdo, A. A., Ackermann, M., et al. 2012, *ApJS*, 199, 31, doi: [10.1088/0067-0049/199/2/31](https://doi.org/10.1088/0067-0049/199/2/31)
- Peirson, A. L., & Romani, R. W. 2019, *ApJ*, 885, 76, doi: [10.3847/1538-4357/ab46b1](https://doi.org/10.3847/1538-4357/ab46b1)
- Peng, F.-K., Zhang, H.-M., Wang, X.-Y., Wang, J.-F., & Zhi, Q.-J. 2019, *ApJ*, 884, 91, doi: [10.3847/1538-4357/ab3e6f](https://doi.org/10.3847/1538-4357/ab3e6f)
- Perley, R. A., Roser, H.-J., & Meisenheimer, K. 1997, *A&A*, 328, 12
- Roeser, H.-J., & Meisenheimer, K. 1987, *ApJ*, 314, 70, doi: [10.1086/165039](https://doi.org/10.1086/165039)
- Rulten, C. B., Brown, A. M., & Chadwick, P. M. 2020, *MNRAS*, 492, 4666, doi: [10.1093/mnras/staa054](https://doi.org/10.1093/mnras/staa054)
- Sahakyan, N., Yang, R., Aharonian, F. A., & Rieger, F. M. 2013, *ApJL*, 770, L6, doi: [10.1088/2041-8205/770/1/L6](https://doi.org/10.1088/2041-8205/770/1/L6)
- Sambruna, R. M., Eracleous, M., & Mushotzky, R. F. 1999, *ApJ*, 526, 60, doi: [10.1086/307981](https://doi.org/10.1086/307981)
- Schmidt, M. 1965, *ApJ*, 141, 1, doi: [10.1086/148085](https://doi.org/10.1086/148085)
- Shaik, A., Meyer, E. T., Reddy, K., Laha, S., & Georganopoulos, M. 2024, arXiv e-prints, arXiv:2402.06218, doi: [10.48550/arXiv.2402.06218](https://doi.org/10.48550/arXiv.2402.06218)
- Simkin, S. M., Sadler, E. M., Sault, R., Tingay, S. J., & Callcut, J. 1999, *ApJS*, 123, 447, doi: [10.1086/313243](https://doi.org/10.1086/313243)
- Singh, K. P., Rao, A. R., & Vahia, M. N. 1990, *MNRAS*, 246, 706
- Stawarz, L., Cheung, C. C., Harris, D. E., & Ostrowski, M. 2007, *The Astrophysical Journal*, 662, 213, doi: [10.1086/517966](https://doi.org/10.1086/517966)
- Strohmayer, T. E. 2017, *ApJ*, 838, 72, doi: [10.3847/1538-4357/aa643d](https://doi.org/10.3847/1538-4357/aa643d)
- Sun, X.-n., Yang, R.-z., Mckinley, B., & Aharonian, F. 2016, *A&A*, 595, A29, doi: [10.1051/0004-6361/201629069](https://doi.org/10.1051/0004-6361/201629069)
- Sunada, Y., Morimoto, A., Tashiro, M. S., et al. 2022, *PASJ*, 74, 602, doi: [10.1093/pasj/psac022](https://doi.org/10.1093/pasj/psac022)
- Tavecchio, F., Cerutti, R., Maraschi, L., et al. 2005, *ApJ*, 630, 721, doi: [10.1086/432371](https://doi.org/10.1086/432371)
- Tavecchio, F., & Ghisellini, G. 2008, *MNRAS*, 385, L98, doi: [10.1111/j.1745-3933.2008.00441.x](https://doi.org/10.1111/j.1745-3933.2008.00441.x)
- Tavecchio, F., Maraschi, L., Sambruna, R. M., & Urry, C. M. 2000, *ApJL*, 544, L23, doi: [10.1086/317292](https://doi.org/10.1086/317292)
- Thimmappa, R., Stawarz, L., Marchenko, V., et al. 2020, *ApJ*, 903, 109, doi: [10.3847/1538-4357/abb605](https://doi.org/10.3847/1538-4357/abb605)
- Thimmappa, R., Stawarz, L., Neilsen, J., Ostrowski, M., & Reville, B. 2022, *ApJ*, 941, 204, doi: [10.3847/1538-4357/aca472](https://doi.org/10.3847/1538-4357/aca472)
- Thomson, R. C., Crane, P., & Mackay, C. D. 1995, *ApJL*, 446, L93, doi: [10.1086/187938](https://doi.org/10.1086/187938)
- Tingay, S. J., Lenc, E., Brunetti, G., & Bondi, M. 2008, *AJ*, 136, 2473, doi: [10.1088/0004-6256/136/6/2473](https://doi.org/10.1088/0004-6256/136/6/2473)
- Tingay, S. J., Jauncey, D. L., Reynolds, J. E., et al. 2000, *AJ*, 119, 1695, doi: [10.1086/301283](https://doi.org/10.1086/301283)
- Wang, X.-Y., Bi, X.-J., Cao, Z., et al. 2022, *Chinese Physics C*, 46, 030003, doi: [10.1088/1674-1137/ac3fa9](https://doi.org/10.1088/1674-1137/ac3fa9)
- Wang, Z.-J., Zhang, J., Sun, X.-N., & Liang, E.-W. 2020, *ApJ*, 893, 41, doi: [10.3847/1538-4357/ab7d35](https://doi.org/10.3847/1538-4357/ab7d35)
- Weisskopf, M. 2022, in *AAS/High Energy Astrophysics Division*, Vol. 54, AAS/High Energy Astrophysics Division, 301.01
- Wilson, A. S., Young, A. J., & Shopbell, P. L. 2001, *ApJ*, 547, 740, doi: [10.1086/318412](https://doi.org/10.1086/318412)
- Wood, M., Caputo, R., Charles, E., et al. 2017, in *International Cosmic Ray Conference*, Vol. 301, 35th International Cosmic Ray Conference (ICRC2017), 824, doi: [10.22323/1.301.0824](https://doi.org/10.22323/1.301.0824)
- Wright, E. L., Eisenhardt, P. R. M., Mainzer, A. K., et al. 2010, *AJ*, 140, 1868, doi: [10.1088/0004-6256/140/6/1868](https://doi.org/10.1088/0004-6256/140/6/1868)
- Xie, F., Wong, J., La Monaca, F., et al. 2024, *ApJ*, 962, 92, doi: [10.3847/1538-4357/ad17ba](https://doi.org/10.3847/1538-4357/ad17ba)
- Xue, Z.-W., Zhang, J., Cui, W., Liang, E.-W., & Zhang, S.-N. 2017, *Research in Astronomy and Astrophysics*, 17, 090, doi: [10.1088/1674-4527/17/9/90](https://doi.org/10.1088/1674-4527/17/9/90)
- Yu, Y.-W., Zhang, H.-M., Gan, Y.-Y., et al. 2024, *ApJ*, 965, 163, doi: [10.3847/1538-4357/ad2e07](https://doi.org/10.3847/1538-4357/ad2e07)
- Zhang, J., Bai, J. M., Chen, L., & Liang, E. 2010, *ApJ*, 710, 1017, doi: [10.1088/0004-637X/710/2/1017](https://doi.org/10.1088/0004-637X/710/2/1017)
- Zhang, J., Bai, J. M., Chen, L., & Yang, X. 2009, *ApJ*, 701, 423, doi: [10.1088/0004-637X/701/1/423](https://doi.org/10.1088/0004-637X/701/1/423)
- Zhang, J., Du, S.-s., Guo, S.-C., et al. 2018, *ApJ*, 858, 27, doi: [10.3847/1538-4357/aab9b2](https://doi.org/10.3847/1538-4357/aab9b2)
- Zhang, J., Liang, E.-W., Zhang, S.-N., & Bai, J. M. 2012, *ApJ*, 752, 157, doi: [10.1088/0004-637X/752/2/157](https://doi.org/10.1088/0004-637X/752/2/157)

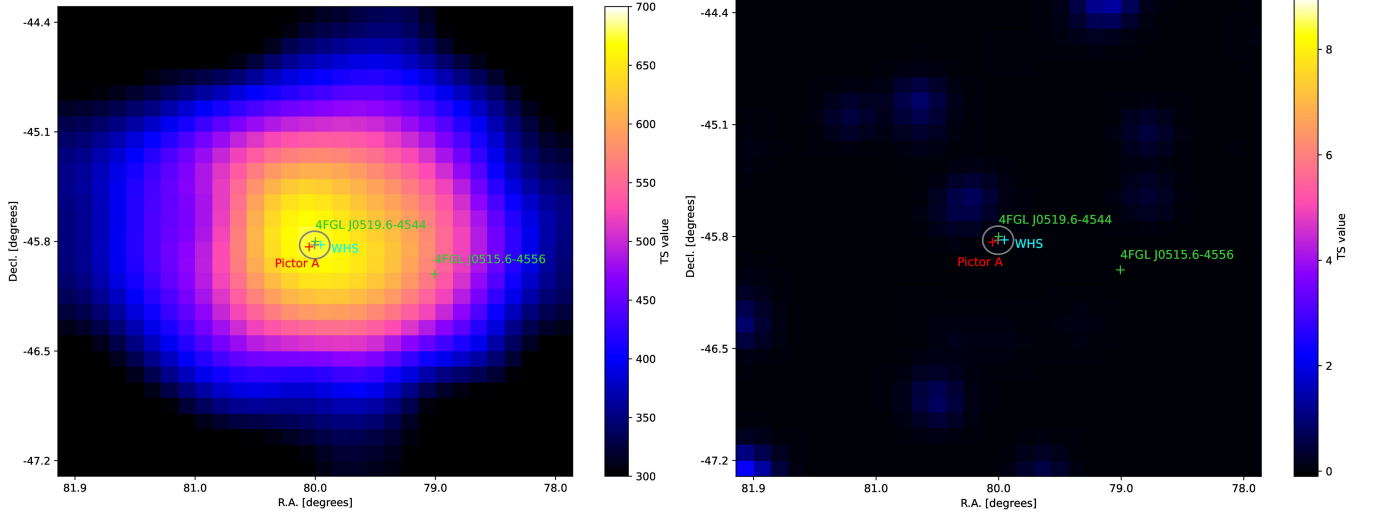


**Figure 1.**  $3^\circ \times 3^\circ$  TS map (left panel) and residual TS map (right panel) of Pictor A in the 0.1–500 GeV band. The green crosses represent the positions of 4FGL J0519.6-4544 and 4FGL J0515.6-4556 in the 4FGL-DR4. The red and cyan crosses represent the radio position of Pictor A and the Chandra pointing position (Wilson et al. 2001) of WHS, respectively. The grey cross and grey circle represent the best-fit position of  $\gamma$ -ray source in this work along with its corresponding 95% containment region.

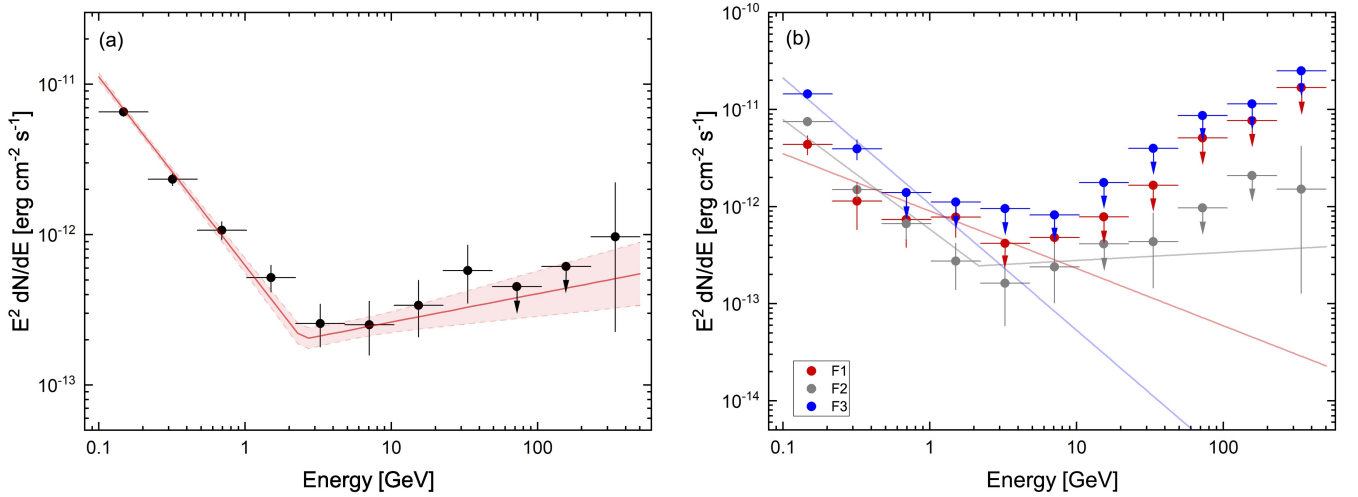


**Figure 2.** The Fermi-LAT spectra for Pictor A in the 0.1–500 GeV band. Panel (a): the  $\sim 16$ -year average spectrum. Panel (b): the spectra of three high/low states, corresponding to the three regions shaded in different colors in Figure 3(a). The  $2\sigma$  upper limit (points with a downward arrow) is reported when  $TS \leq 4$  for that energy bin. The color lines represent the corresponding best-fit results using either a BPL or a PL function. The pink shaded region in Panel (a) indicates the  $1\sigma$  uncertainty of the fitting result.

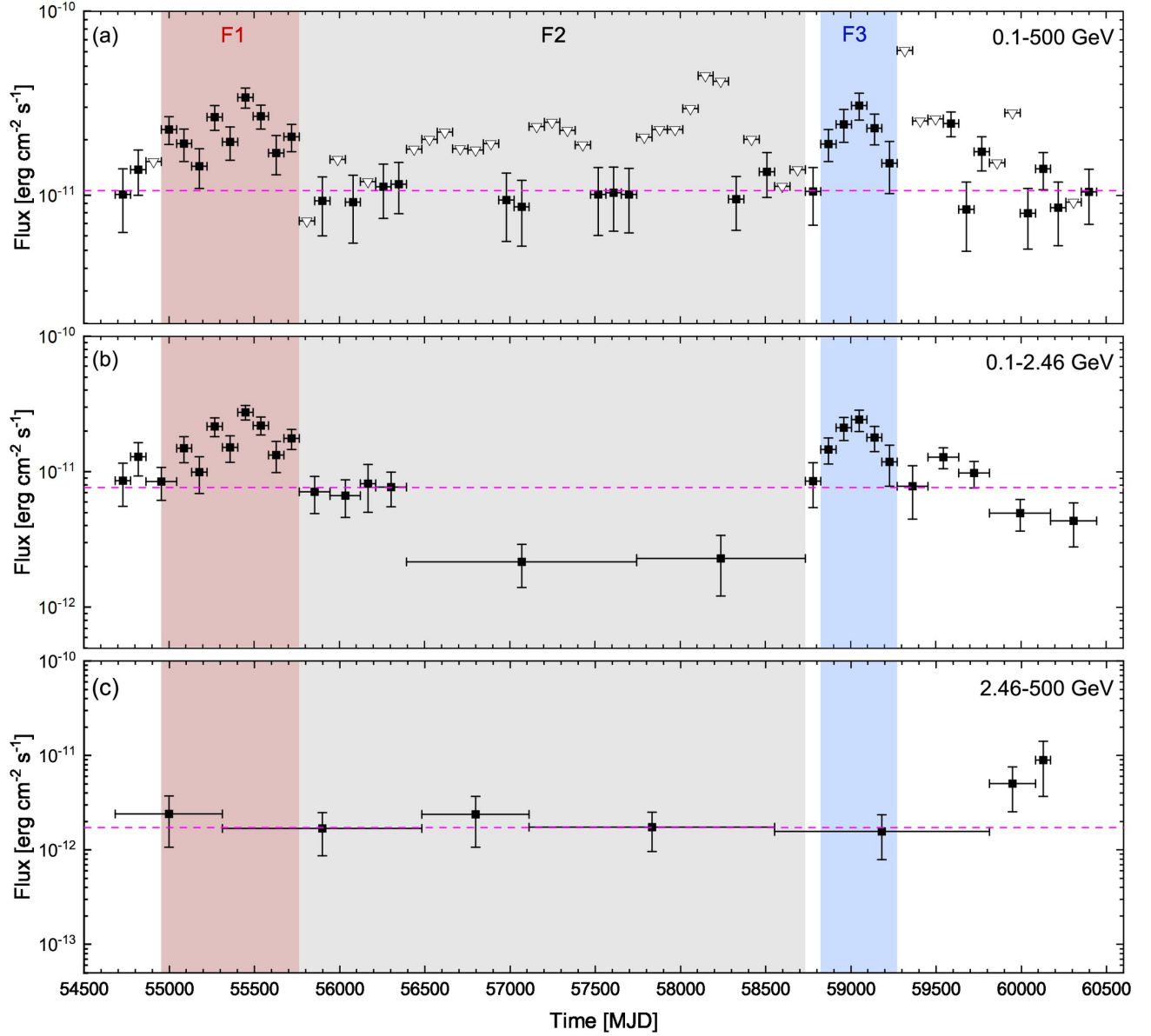


**Figure 3.** The long-term light curves of Pictor A, derived with the  $\sim 16$ -year Fermi-LAT observation data in different energy bands, including the 0.1–500 GeV band (Panel (a)) together with the energy bands below (0.1–2.46 GeV in Panel (b)) and above (2.46–500 GeV in Panel (c)) the spectral break. The horizontal magenta dashed lines represent the average flux in that energy band. In panel (a), each time bin is 90 days, and the  $3\sigma$  upper limit, denoted by open inverted triangles, is reported for time bins where  $TS \leq 9$ . In panels (b) and (c), the light curves are derived with an adaptive-binning method based on a criterion of  $TS \geq 9$  for each time bin, where the minimum time bin is 90 days.

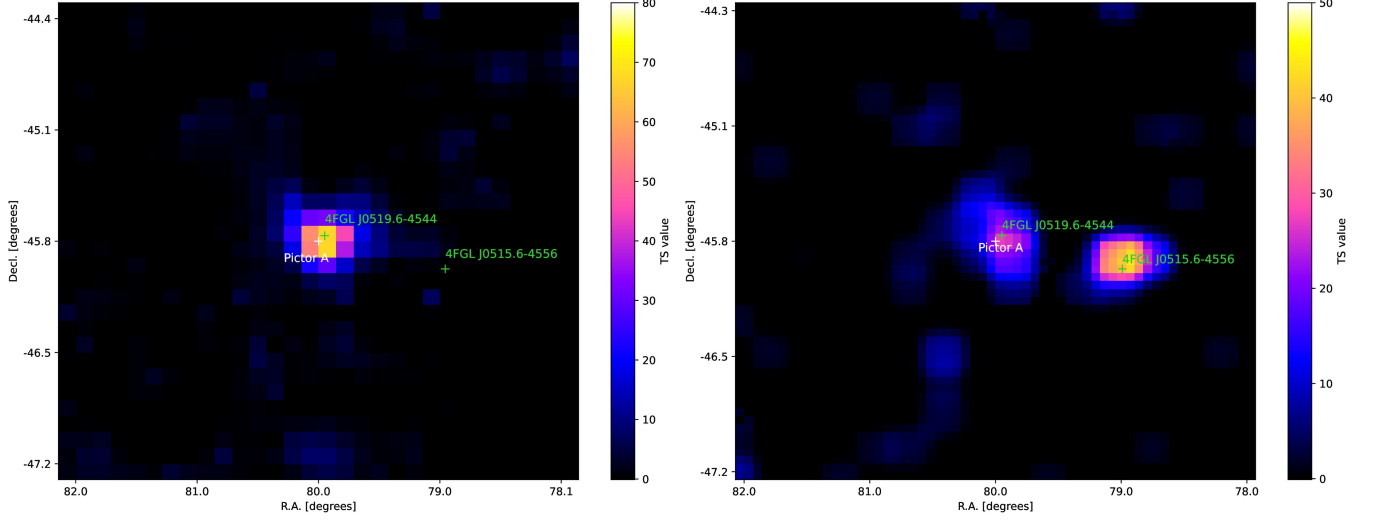


**Figure 4.** Left panel:  $3^\circ \times 3^\circ$  residual TS map in the 2.0–500 GeV band by removing 4FGL J0519.6–4544 (associated with Pictor A) from the *model.xml*. Right panel:  $3^\circ \times 3^\circ$  TS map of Pictor A and PKS J0515–4556 in the 20.0–500 GeV band. The green crosses represent the positions of 4FGL J0519.6–4544 and 4FGL J0515.6–4556 in the 4FGL-DR4 (Abdollahi et al. 2022; Ballet et al. 2023). The white crosses represent the radio position of Pictor A.

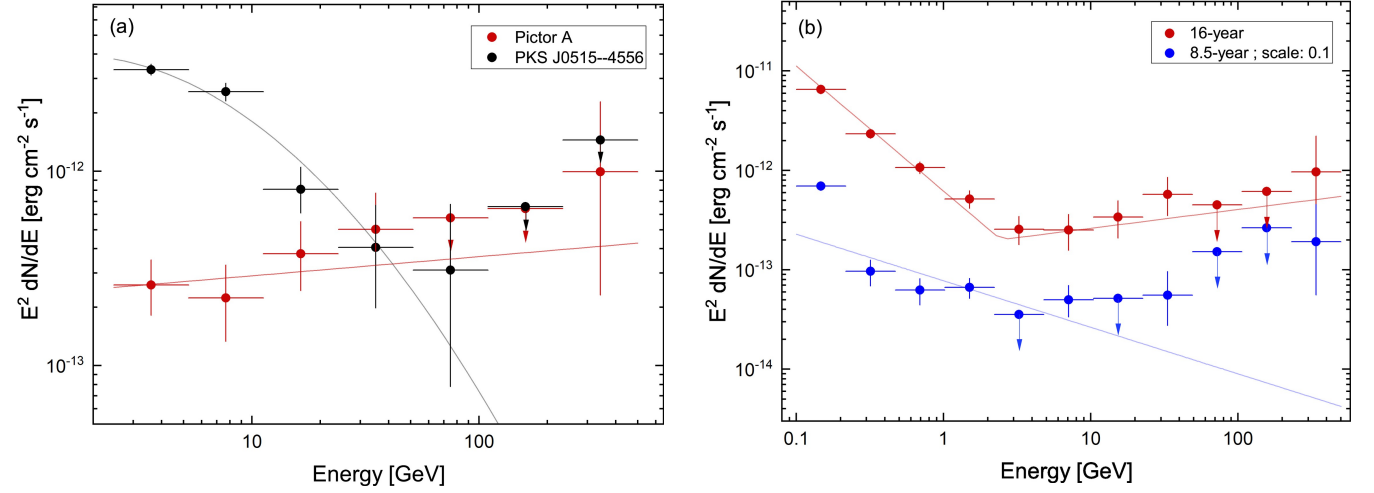


**Figure 5.** Panel (a): The spectra of Pictor A (red symbols) and PKS J0515–4556 (black symbols) in the 2.46–500 GeV band of 16-year dataset. Panel (b): The  $\gamma$ -ray spectra of Pictor A in the 0.1–500 GeV energy band for different observation durations: red symbols represent the 16-year dataset and blue symbols represent the first 8.5-year dataset. For clarity of comparison, the spectrum of the 8.5-year dataset has been scaled by a factor of 0.1. The  $2\sigma$  upper limit (points with a downward arrow) is reported when  $TS \leq 4$  for that energy bin in both panel (a) and (b).

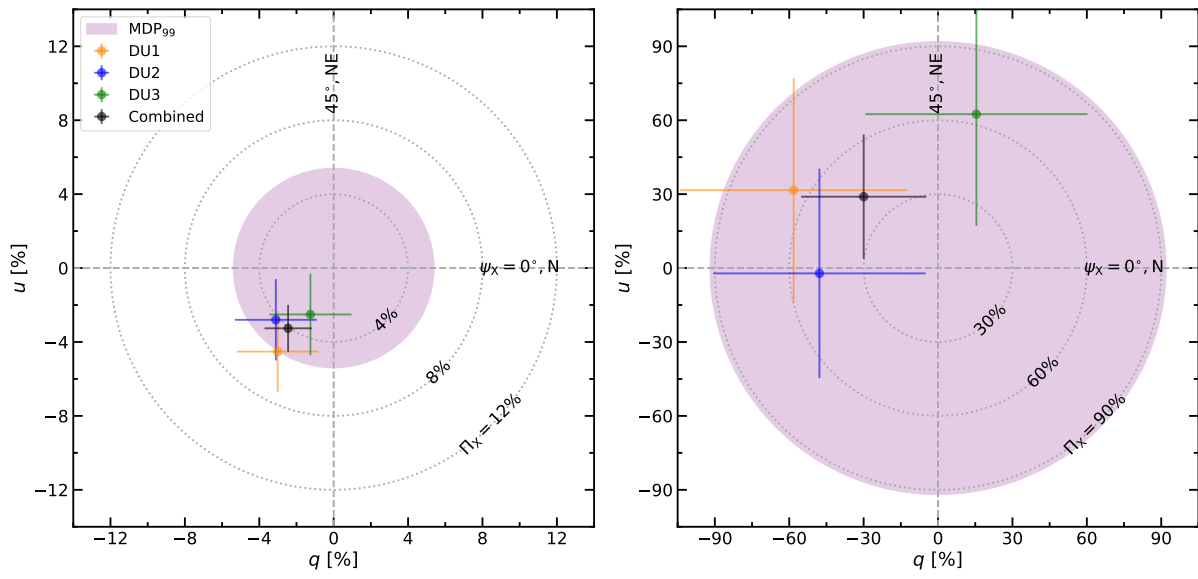


**Figure 6.** Normalized Stokes parameters  $q$  and  $u$  of the nucleus (left panel) and WHS (right panel) in the 2–8 keV band for different DUs, as measured using the PCUBE algorithm in software `ixpeobssim`.

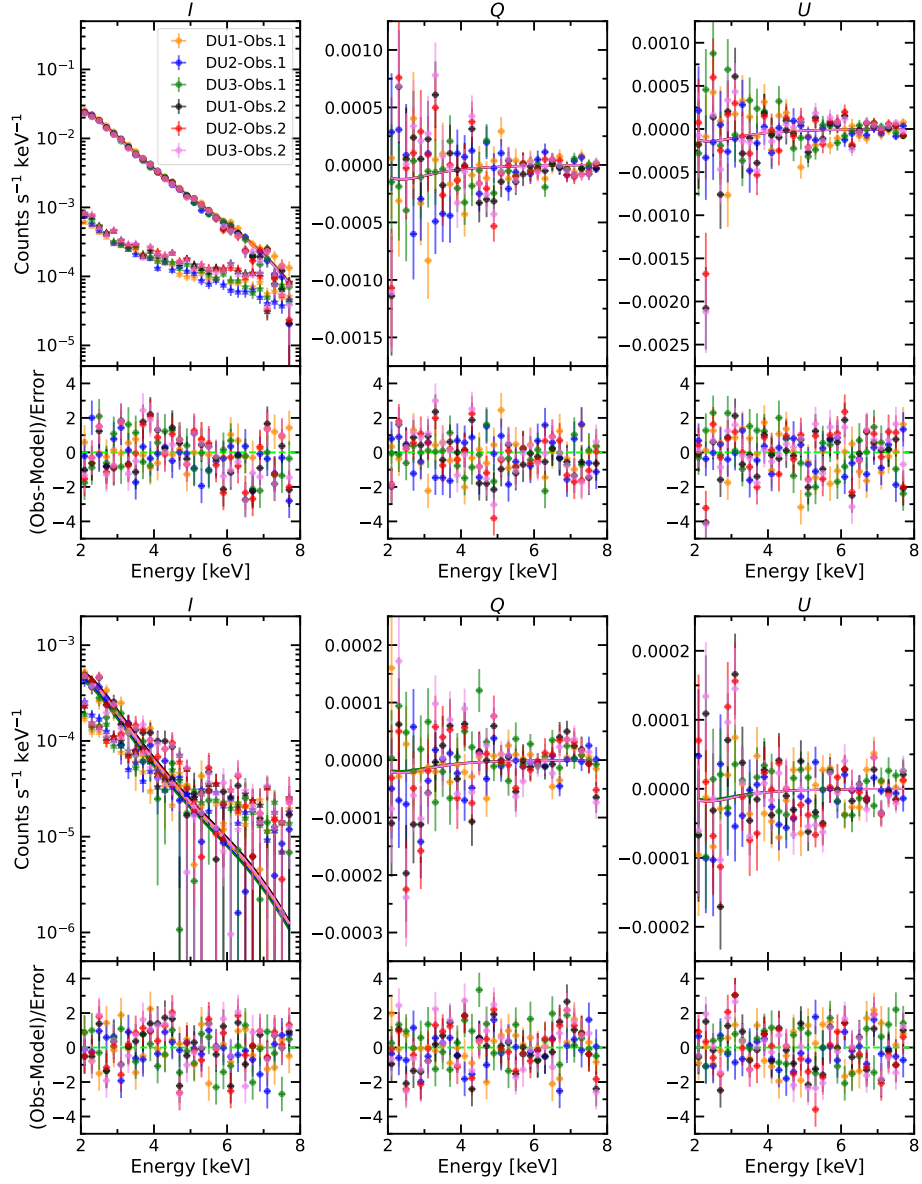


**Figure 7.** Spectropolarimetric fit results for the nucleus (top panel) and WHS (bottom). Panels represent the fits to the IXPE Stokes parameters  $I$ ,  $Q$ , and  $U$  with their associated residuals from left to right. In the  $I$  spectra panels, the triangles indicate the background spectra for different DUs.

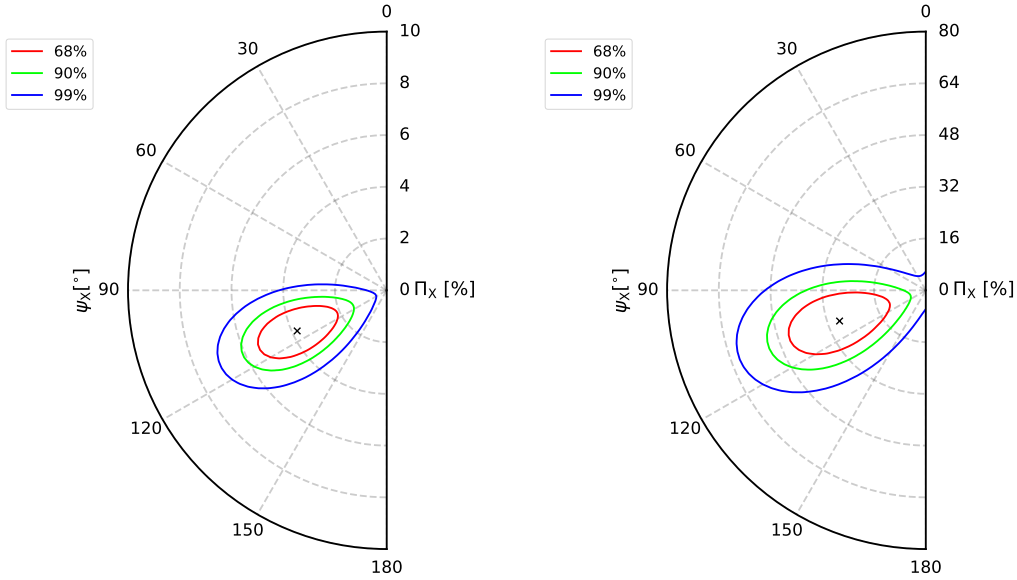


**Figure 8.** X-ray polarization contours in the 2–8 keV energy band for the nucleus (left panel) and WHS (right panel), derived from the spectropolarimetric fitting using *Xspec*. The black crosses represent the best-fit values of  $\Pi_X$  and  $\psi_X$ . The red, green, and blue contours denote the 68%, 90%, and 99% confidence intervals, respectively.

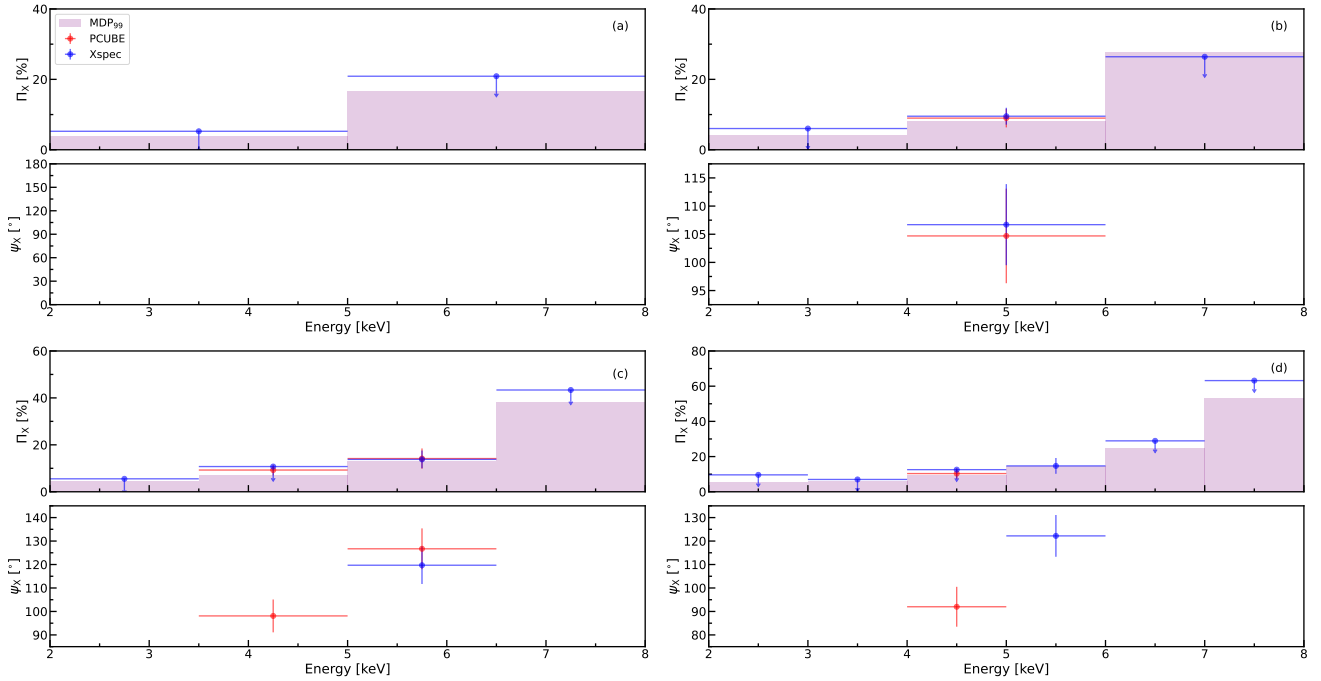


**Figure 9.** Results of energy-resolved analysis for the polarization of the nucleus in different energy bins: panel (a) for 3 keV  $\text{bin}^{-1}$ , panel (b) for 2 keV  $\text{bin}^{-1}$ , panel (c) for 1.5 keV  $\text{bin}^{-1}$  and panel (d) for 1 keV  $\text{bin}^{-1}$ , respectively. In each panel, the red points represent the results estimated via *PCUBE* algorithm in *ixpeobssim*, the blue points represent the results estimated via spectropolarimetric fits in *Xspec*, and the violet shaded areas represent the  $\text{MDP}_{99}$  values for different energy bins. Particularly, if the best-fit value of  $\Pi_X$  from spectropolarimetric fit is lower than the associated value of  $\text{MDP}_{99}$ , an upper limit at the 99% confidence level will be provided, marked by blue points with down-arrows.

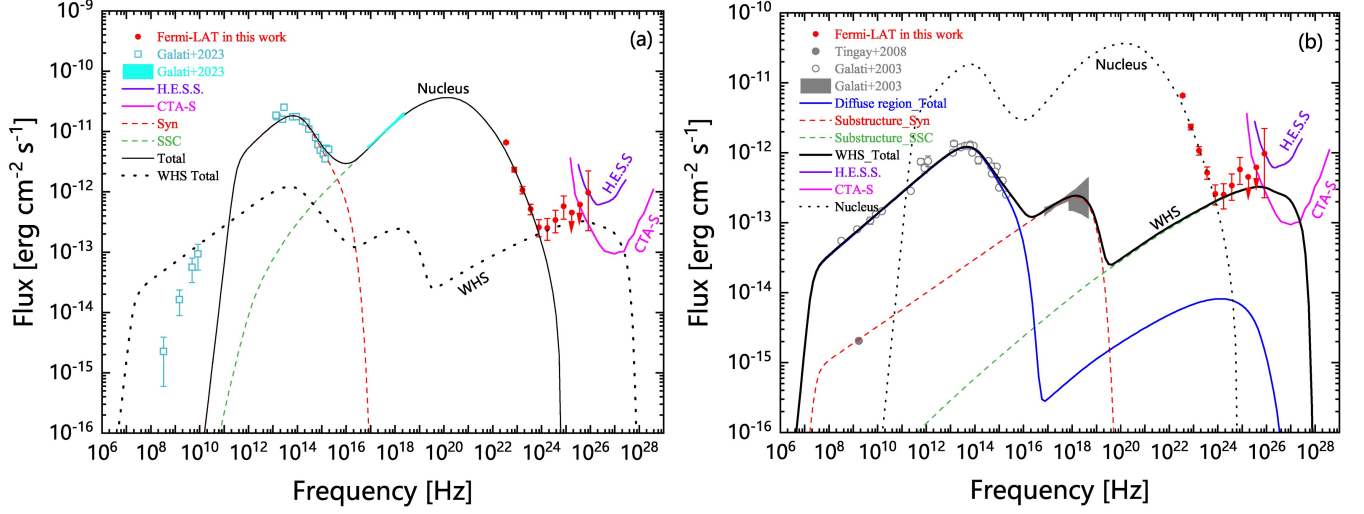


**Figure 10.** Observed SEDs with model fitting for the nucleus (Panel (a)) and the WHS (Panel (b)) in Pictor A. The data from radio to X-rays for both the nucleus and WHS are taken from [Gulati et al. \(2023\)](#) and the references therein; for the WHS, including the radio and optical data from [Meisenheimer et al. \(1997\)](#), the IR and the substructure data from [Tingay et al. \(2008\)](#), the mid-infrared data from [Isobe et al. \(2017\)](#), two optical/near-ultraviolet points from [Wilson et al. \(2001\)](#), the far-infrared data from [Isobe et al. \(2020\)](#), and the NuSTAR spectrum from [Sunada et al. \(2022\)](#); for the nucleus, including the radio data from [Perley et al. \(1997\)](#), the IR data from [Singh et al. \(1990\)](#), and the mid-infrared data from ([Wright et al. 2010](#); [Cutri et al. 2013](#)). It should be noted that this work takes into consideration the X-ray spectrum of the nucleus in a high-flux state, which is different from that in [Gulati et al. \(2023\)](#). The Fermi-LAT spectrum is derived from the analysis conducted in this study, same as in Figure 2(a).

**Table 1.** Spectral Fitting Results of Fermi-LAT Observations for Pictor A

Time range (MJD)	Energy range (GeV)	Model	$\Gamma_{\gamma,1}$	$\Gamma_{\gamma,2}$	$E_b$ (GeV)	Flux ( $\times 10^{-12}$ erg cm $^{-2}$ s $^{-1}$ )	TS
(1)	(2)	(3)	(4)	(5)	(6)	(7)	(8)
Full time	0.1–500	PL	$3.05 \pm 0.08$	–	–	$8.98 \pm 0.73$	669.55
(54682–60501)	0.1–500	BPL	$3.25 \pm 0.15$	$1.81 \pm 0.07$	$2.46 \pm 0.09$	$10.61 \pm 0.82$	773.10
	0.1–2.46	PL	$3.12 \pm 0.06$	–	–	$7.68 \pm 0.82$	541.21
	2.46–500	PL	$1.97 \pm 0.18$	–	–	$1.72 \pm 0.56$	64.06
F1 (54952–55762)	0.1–500	PL	$2.59 \pm 0.21$	–	–	$5.91 \pm 1.56$	50.95
F2 (55762–58732)	0.1–500	BPL	$3.13 \pm 0.08$	$1.92 \pm 0.16$	$2.15 \pm 0.27$	$8.47 \pm 1.05$	241.27
F3 (58822–59272)	0.1–500	PL	$3.30 \pm 0.17$	–	–	$16.34 \pm 2.87$	156.39

Column (1): Time range for spectral fitting; Column (2): Energy range for spectral fitting; Column (3): Spectral function utilized in fitting; Columns (4) and (5): Photon spectral indices for PL or BPL functions; Column (6): Break energy for the BPL model; Column (7): Average flux in the corresponding energy band and time period; Column (8): TS value in the corresponding energy band and time period.

**Table 2.** Information for Each Time Bin of the Light Curve in Energy Bands 0.1–2.46 GeV and 2.46–500 GeV

Bin number	Time.start (MJD)	Time.end (MJD)	bin size (days)	Flux ( $\text{erg cm}^{-2} \text{s}^{-1}$ )	Flux error ( $\text{erg cm}^{-2} \text{s}^{-1}$ )	TS
(1)	(2)	(3)	(4)	(5)	(6)	(7)
Energy band within 0.1–2.46 GeV						
1	54682.66	54772.66	90	$8.59 \times 10^{-12}$	$3.02 \times 10^{-12}$	9.96
2	54772.66	54862.66	90	$1.29 \times 10^{-11}$	$3.57 \times 10^{-12}$	22.20
3	54862.66	55042.66	180	$8.48 \times 10^{-12}$	$2.30 \times 10^{-12}$	20.29
4	55042.66	55132.66	90	$1.49 \times 10^{-11}$	$3.23 \times 10^{-12}$	30.27
5	55132.66	55222.66	90	$9.92 \times 10^{-12}$	$3.00 \times 10^{-12}$	16.31
6	55222.66	55312.66	90	$2.16 \times 10^{-11}$	$3.40 \times 10^{-12}$	55.85
7	55312.66	55402.66	90	$1.51 \times 10^{-11}$	$3.35 \times 10^{-12}$	28.32
8	55402.66	55492.66	90	$2.75 \times 10^{-11}$	$3.43 \times 10^{-12}$	100.04
9	55492.66	55582.66	90	$2.20 \times 10^{-11}$	$3.29 \times 10^{-12}$	62.75
10	55582.66	55672.66	90	$1.33 \times 10^{-11}$	$3.45 \times 10^{-12}$	23.37
11	55672.66	55762.66	90	$1.76 \times 10^{-11}$	$3.02 \times 10^{-12}$	50.97
12	55762.66	55942.66	180	$7.10 \times 10^{-12}$	$2.17 \times 10^{-12}$	15.72
13	55942.66	56122.66	180	$6.68 \times 10^{-12}$	$2.07 \times 10^{-12}$	15.88
14	56122.66	56212.66	90	$8.17 \times 10^{-12}$	$3.14 \times 10^{-12}$	9.92
15	56212.66	56392.66	180	$7.74 \times 10^{-12}$	$2.21 \times 10^{-12}$	19.80
16	56392.66	57742.66	1350	$2.16 \times 10^{-12}$	$7.59 \times 10^{-13}$	12.49
17	57742.66	58732.66	990	$2.30 \times 10^{-12}$	$1.09 \times 10^{-12}$	9.37
18	58732.66	58822.66	90	$8.56 \times 10^{-12}$	$3.11 \times 10^{-12}$	11.73
19	58822.66	58912.66	90	$1.46 \times 10^{-11}$	$3.20 \times 10^{-12}$	33.36
20	58912.66	59002.66	90	$2.11 \times 10^{-11}$	$4.12 \times 10^{-12}$	44.33
21	59002.66	59092.66	90	$2.42 \times 10^{-11}$	$4.32 \times 10^{-12}$	61.51
22	59092.66	59182.66	90	$1.79 \times 10^{-11}$	$3.77 \times 10^{-12}$	37.16
23	59182.66	59272.66	90	$1.18 \times 10^{-11}$	$3.96 \times 10^{-12}$	17.08
24	59272.66	59452.66	180	$7.80 \times 10^{-12}$	$3.32 \times 10^{-12}$	13.54
25	59452.66	59632.66	180	$1.28 \times 10^{-11}$	$2.25 \times 10^{-12}$	54.31
26	59632.66	59812.66	180	$9.78 \times 10^{-12}$	$2.17 \times 10^{-12}$	33.65
27	59812.66	60172.66	360	$4.96 \times 10^{-12}$	$1.31 \times 10^{-12}$	22.08
28	60172.66	60442.66	270	$4.35 \times 10^{-12}$	$1.57 \times 10^{-12}$	11.46
Energy band within 2.46–500 GeV						
1	54682.66	55312.66	630	$2.40 \times 10^{-12}$	$1.33 \times 10^{-12}$	9.49
2	55312.66	56482.66	1170	$1.68 \times 10^{-12}$	$8.14 \times 10^{-13}$	10.41
3	56482.66	57112.66	630	$2.37 \times 10^{-12}$	$1.30 \times 10^{-12}$	9.79
4	57112.66	58552.66	1440	$1.74 \times 10^{-12}$	$7.77 \times 10^{-13}$	9.94
5	58552.66	59812.66	1260	$1.57 \times 10^{-12}$	$7.77 \times 10^{-13}$	9.81
6	59812.66	60082.66	270	$5.04 \times 10^{-12}$	$2.50 \times 10^{-12}$	10.82
7	60082.66	60172.66	90	$8.90 \times 10^{-12}$	$5.20 \times 10^{-12}$	11.17

Column (1): Serial number of this time bin; Column (2): Time-bin start time; Column (3): Time-bin end time; Column (4): Duration of the corresponding time bin; Column (5): Average flux in corresponding time bin; Column (6): Corresponding error of the average flux; Column (7): TS value in the corresponding time bin.

**Table 3.** Results of the Spectropolarimetric Analysis in the 2–8 keV Band for Both the Nucleus and WHS

Component	Parameter	Unit	Value	
			Nucleus	WHS
Model = CONSTANT×TBABS×POWERLAW				
CONSTANT	$C_{\text{DU1-Obs.1}}$		1.0 (fixed)	1.0 (fixed)
	$C_{\text{DU2-Obs.1}}$		$1.048 \pm 0.009$	$1.039^{+0.094}_{-0.087}$
	$C_{\text{DU3-Obs.1}}$		$1.021 \pm 0.009$	$0.983^{+0.091}_{-0.084}$
	$C_{\text{DU1-Obs.2}}$		$0.947 \pm 0.008$	$1.129^{+0.097}_{-0.089}$
	$C_{\text{DU2-Obs.2}}$		$1.029 \pm 0.009$	$1.202^{+0.104}_{-0.096}$
	$C_{\text{DU3-Obs.2}}$		$1.017 \pm 0.009$	$1.160^{+0.102}_{-0.094}$
TBABS	$N_{\text{H}}$	$10^{20} \text{ cm}^{-2}$	3.62 (fixed)	3.57 (fixed)
POWERLAW	$\Gamma_{\text{X}}$		$1.84 \pm 0.01$	$2.07 \pm 0.11$
	$N_0$	$10^{-3} \text{ ph keV}^{-1} \text{ cm}^{-2} \text{ s}^{-1}$	$4.92 \pm 0.06$	$0.11 \pm 0.01$
Fit Statistic	$\chi^2/\text{dof}$		233/167	210/167
Model = CONSTANT×TBABS×POLCONST×POWERLAW				
POLCONST	$\Pi_{\text{X}}$	%	< 6.6	< 56.4
	$\psi_{\text{X}}$	°	...	...
Fit Statistic	$\chi^2/\text{dof}$		721/520	714/520

**Table 4.** Parameters of SED Fitting for both the Nucleus and WHS

Parameter	Symbol	Nucleus	WHS	
			Diffuse	Substructure
Electron density parameter	$N_0 [\text{cm}^{-3}]$	$6.5 \times 10^5$	$2.6 \times 10^{-3}$	49
Spectral index below break	$p_1^*$	2.2	2.4	2.52
Spectral index above break	$p_2^*$	4.42	4.1	
Minimum electron Lorentz factor	$\gamma_{\text{min}}^*$	1	1	1
Break Lorentz factor	$\gamma_{\text{b}}$	$1.6 \times 10^3$	$2.2 \times 10^5$	
Maximum electron Lorentz factor	$\gamma_{\text{max}}$	$1.6 \times 10^4$	$2.2 \times 10^6$	$2.1 \times 10^8$
Radius of the blob	$R^* [\text{cm/pc}]$	$10^{16} \text{ cm}$	500 pc	30 pc
Bulk Lorentz factor	$\Gamma^*$	5	1	1
Doppler boosting factor	$\delta^*$	1.3	1	1
Magnetic Field	$B [\text{G}]$	7	$3.6 \times 10^{-4}$	$3.5 \times 10^{-5}$
Equipartition ratio	$U_e/U_B$	1.08	1	$1.6 \times 10^6$

\*The parameters remain fixed during SED modeling.